Mesoarchean partial melting of mafic crust and tonalite production during high-T–low-P stagnant tectonism, Akia Terrane, West Greenland

C. Yakymchuk[a,*], C.L. Kirkland[b], J.A. Hollis[c], J. Kendrick[a], N.J. Gardiner[d,e], K. Szilas[f]

[a] Department of Earth and Environmental Sciences, University of Waterloo, Waterloo, Ontario N2L 3G1, Canada
[b] School of Earth and Planetary Science, Centre for Exploration Targeting – Curtin Node, Curtin University, Perth, Western Australia 6102, Australia
[c] Department of Geology, Ministry of Mineral Resources and Labour, Government of Greenland, P.O. Box 930, 3900 Nuuk, Greenland
[d] School of Earth, Atmosphere, and Environment, Monash University, Melbourne, Australia
[e] School of Earth and Environmental Sciences, University of St., Andrews, St. Andrews, UK
[f] Department of Geosciences and Natural Resource Management, University of Copenhagen, Øster Voldgade 10, DK-13 450 Copenhagen K, Denmark

ARTICLE INFO

ABSTRACT

Different geodynamic models exist for the growth and differentiation of Archean continental crust, ranging from horizontal tectonics with subduction zones to vertical tectonics with foundering of greenstone sequences. U–Pb zircon geochronology, field relationships, and pressure–temperature constraints from granulite-facies metabasite of the Akia Terrane of the North Atlantic Craton in West Greenland show that this terrane grew through two major magmatic growth episodes: an earlier one at c. 3.2 Ga, and a later one at c. 3.05–2.97 Ga. Phase equilibrium modelling for assemblages related to the latter indicates temperatures of > 800 °C at < 0.9 GPa, consistent with a high apparent geothermal gradient and implies thin crust. Granulite-facies metamorphism and partial melting occurred in the absence of pervasive ductile deformation as indicated by nebulitic, undeformed pyroxene-bearing leucosome in metabasite gneiss. Trace element modelling suggests that c. 3.0 Ga tonalite at the current exposure level in the Akia Terrane was generated at pressures of > 0.8 GPa in the stability field of garnet. U–Pb zircon geochronology and existing Hf isotope data are also consistent with a model involving protracted Mesoarchean magmatic growth with limited mantle addition during a prolonged period of high temperatures in a relatively stagnant tectonic regime prior to Neoarchean compressional tectonism in the Akia Terrane.

1. Introduction

Much of the continental crust on Earth was generated in the Archean (e.g. Dhuime et al., 2012; Belousova et al., 2010; Rudnick and Gao, 2014; Condie et al., 2016), but whether this occurred via Phanerozoic-like tectonic processes, or in alternative settings in a subduction zone-free environment is debated (e.g. Hamilton, 2011; Wyman, 2013; 2018; Bédard et al., 2013; Johnson et al., 2017; Bédard, 2018; Palin and Dyck, 2018). Modern continental crust is thought to be generated at subduction zones through the accretion of oceanic arcs, and through supra subduction-zone magmatism. In contrast, Archean cratons are dominated by sodic tonalite–trondhjemite–granodiorite (TTG) suites that are commonly tectonically reworked with metabasic rocks to result in composite grey gneiss (e.g. Moyen and Martin, 2012; White et al., 2017). TTGs are derived from the partial melting of hydrated mafic rocks (e.g. Rapp et al., 1991; Moyen and Martin, 2012; Nagel et al., 2012; Martin et al., 2014; Moyen and Laurent, 2018), and

the rarity of similar rocks in the Phanerozoic has triggered three principal geodynamic models for the generation of Archean continental crust: (1) melting of subducted oceanic crust due to a hotter ambient mantle (e.g. Hastie et al., 2010), (2) reworking of juvenile oceanic plateaux driven by periodic mantle overturn and not through subduction (e.g. Smithies et al., 2005; Bédard, 2006; 2018; Sizova et al., 2010, 2015; Johnson et al., 2014), or (3) melting at the base of tectonically thickened arc (Nagel et al., 2012). Differentiating between these models is complicated by the fragmentary and complex rock archive, but of clear importance in our understanding of the construction and evolution of Earth's first stable continental crust. However, it may be that all processes operated concurrently in different regions (c.f. van Kranendonk, 2010) or that there was a transition between vertically and horizontally driven tectonics in particular areas (e.g. Laurent et al., 2019).

Rare exposures of deep Archean crust provide critical opportunities to investigate the processes that reworked juvenile Archean rocks into

---

more evolved stable continental crust, and to test and refine contrasting models of Precambrian and Phanerozoic crustal evolution. The North Atlantic Craton is made up of several Eoarchean to Neoarchean terranes, including one of the largest exposures of mid- to lower-crustal, Archean amphibolite and mafic granulite (Garde, 1990; Friend and Nutman, 1994; Friend et al., 1996; Friend and Nutman, 2005). The Mesoarchean era represents the primary timeframe for crustal growth in West Greenland, which is a substantial component of the North Atlantic Craton. In the Mesoarchean Akia Terrane of the North Atlantic Craton, the apparent coeval timing of granulite-facies metamorphism and generation of extensive tonalitic crust implies that deep crustal granulite-facies metabasite are a potential source of the tonalite. However, this interpretation is based on U–Pb geochronology and thermobarometry of a limited number of samples.

In this contribution, we use U–Pb zircon geochronology, whole-rock geochemistry as well as phase equilibrium and trace element modelling to evaluate the timing and duration of high-temperature metamorphism and investigate the implications for the source of Mesoarchean tonalite magmatism in the Akia Terrane of West Greenland. The low-pressure (*P*)–high-temperature (*T*) conditions of anatexis coupled with evidence for a prolonged thermal event in this terrane are compatible with a stagnant lid or extensional tectonic regime. Trace element modelling also shows that the concentrations of rare earth elements in c. 3.0 Ga tonalite can be generated by partial melting at the base of the crust and do not require melting of a subducted slab. This evidence suggests that the Mesoarchean tectonic history of the Akia Terrane may have not been solely controlled by singular terrane accretion and arc-related magmatic processes. Therefore, Phanerozoic-style plate tectonics may not be an appropriate geodynamic mode to explain the formation of Mesoarchean terranes of the North Atlantic Craton.

2. Geological setting

2.1. Regional geology

The Akia Terrane extends to the north of Nuuk in West Greenland (Fig. 1). Garde et al. (2000) proposed that the Akia Terrane developed by formation of a 3076–≤3068 Ma magmatic arc, including tholeiitic basalts and calc-alkaline andesites (Garde, 2007; Polat et al., 2015; Szilas et al. 2017), over a c. 3.2 Ga dioritic crustal core, followed by voluminous emplacement of Mesoarchean TTG and dioritic gneiss and synchronous low-pressure granulite-facies metamorphism (Riciputi et al., 1990; Friend and Nutman, 1994; Garde et al., 2000) as well as late-tectonic felsic magmatism. In addition, other researchers (Garde et al. 2012a, 2014; Scherstén and Garde, 2013; Keulen et al., 2015) suggested that a giant bolide impact at ≥3000 Ma was responsible for a prolonged Mesoarchean thermal event, resulting in a range of melting and cataclastic features in the region. Gardiner et al. (2019) recently reported U–Pb zircon ages coupled with in situ Hf-isotope data for TTG gneiss from across the northern Akia Terrane, including samples within the proposed impact-affected area, and showed that these units are indistinguishable and thus inconsistent with the bolide model. Further, Gardiner et al. (2019) suggested that TTG was derived from the melting of basic crust at variable depths that does not require a subduction origin.

Supracrustal units in the region deposited between c. 2877 and 2857 Ma record subsequent high-temperature metamorphism and partial melting during Neoarchean ductile deformation at c. 2857–2700 Ma (Kirkland et al., 2018a). This may be, at least in part, correlative with the tectonic assembly of Paleo- to Neoarchean terranes of the Nuuk region at c. 2720 Ma (Friend and Nutman 2005; Nutman and Friend 2007; Dziggel et al., 2014). A further younger metamorphic event in the Akia Terrane, at c. 2630 Ma, at > 450 to < 850 °C, is recorded by metamorphic zircon overgrowths and neoblastic apatite (Nutman et al., 2007; Kirkland et al., 2018b) and is synchronous with amphibolite-facies metamorphism also recorded in distinct terranes in

the Nuuk region (Nutman et al., 2007; Nutman and Friend, 2007). Subsequent metamorphism at c. 2560 Ma recorded on the Alanngua peninsula (Fig. 1) was interpreted by Dyck et al. (2015) to record the final assembly of the North Atlantic Craton, whereas this is the timing of post-tectonic suturing of the Nuuk region terranes by the Qôrqut Granite Complex (Nutman et al. 2010).

2.2. Field relationships

The Akia Terrane is dominated by c. 3200 Ma and c. 3050–3000 Ma Mesoarchean felsic orthogneiss that have been intruded into, or tectonically interleaved with, supracrustal rocks and metabasite (e.g. Garde et al. 2000; Garde, 2007). These are intruded by Mesoarchean tonalitic to dioritic rocks of the Finnefjeld and Taserssuaq orthogneiss complexes, and the late-tectonic 2980–2970 Ma Qugssuk and Igánánguit granites (Garde 1997; Garde et al., 2000; Scherstén and Garde, 2013). Regionally, mafic rocks in the Akia Terrane are volumetrically more common than in other parts of the North Atlantic Craton (Allaart, 1982).

The felsic orthogneiss comprise polyphase dioritic to tonalitic orthogneiss that underwent several phases of isoclinal recumbent and upright folding (e.g. Berthelsen, 1962; Garde et al., 1987; Kirkland et al., 2018a) and subsequently experienced brittle deformation during the Paleoproterozoic. Based on cross-cutting intrusive relationships preserved in low-strain domains, the oldest components are dioritic rocks associated with metabasite (Fig. 2a) that were subsequently intruded by voluminous tonalite (Fig. 2b).

Metabasite shows textures ranging from relict magmatic gabbroic to high-strain metamorphic fabrics, defined by recrystallised, elongate amphibole. Metabasite bodies in excess of tens of metres in diameter commonly show strain variations, from typically lower-strain cores to higher strain fabrics and structures, including isoclinal folding, at their margins. In most cases, the protoliths of metabasite are unclear due to pervasive recrystallization and deformation. Outside of low-strain domains (e.g. fold hinges) and cores of larger mafic bodies, metabasite commonly holds a moderate to strong gneissic fabric defined by aligned amphibole. In some cases, such as on the Alanngua peninsula (Fig. 1), these fabrics are correlated with Neoarchean deformation and high-pressure granulite-facies partial melting (Kirkland et al., 2018a).

Some interior regions of metabasite bodies contain coarse-grained orthopyroxeneclinopyroxene-bearing leucosome (Fig. 3a, b). In some cases, leucosome networks have sufficiently disrupted the structural integrity of the rock to produce agmatitic textures, in which individual restite blocks have rotated relative to each other (Fig. 2c). Leucosome networks display this morphology regardless of orientation. Close to the tectonic contacts between metabasite bodies and their host felsic orthogneiss, orthopyroxene associated with the two-pyroxene leucosome have amphibole rims and are elongate within a gneissic fabric (Fig. 2d). On a larger scale, entire metabasite blocks at these margins with the host felsic orthogneiss are also elongate within the gneissic fabric (Fig. 2e) and, in some cases, are isoclinally folded within the fabric (Fig. 2f). These observations are consistent with static granulite-facies partial melting, followed by ductile deformation producing strain partitioning related to rheology contrasts between the more competent metabasite units and the enveloping felsic orthogneiss.

In the Maniitsoq region, defined here as coastal outcrops from Maniitsoq Island in the north to Fiskefjord in the south, metabasite commonly contains pyroxene-bearing leucosome. The presence of anhydrous ferromagnesian minerals (e.g. orthopyroxene, clinopyroxene) in leucosome in high-temperature metamorphic rocks is diagnostic of in situ partial melting (e.g. White et al., 2004; Brown, 2013). Additional evidence for in situ partial melting includes progressive plagioclase-enrichment from the host metabasite toward the leucosome, melt-pooling textures, and grain-size coarsening toward the centre of leucosome (Fig. 3a, b). The preservation of the high-temperature mineral assemblages (e.g. orthopyroxene bearing) is also consistent with the
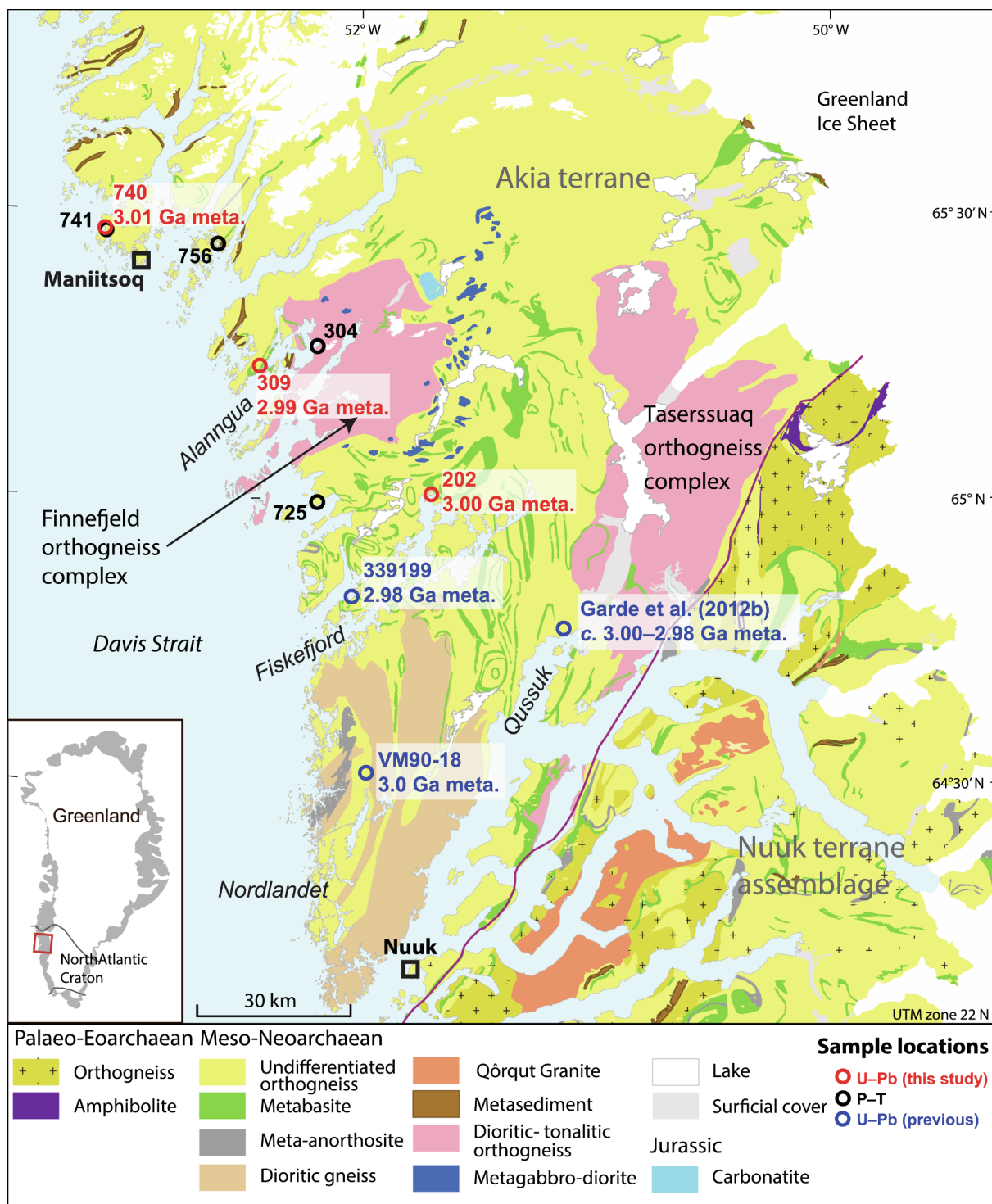
Fig. 1. Map of the Akia and Nuuk terranes of the North Atlantic Craton (modified from Gardiner et al., 2019). Metamorphic U–Pb zircon ages from sample VM90-18 are from Friend and Nutman (1994) and zircon ages from sample 339199 are from Garde et al. (2000). Interpreted U–Pb metamorphic ages of zircon and monazite from the Qussuk peninsula are from Garde et al. (2012b).

loss of anatectic melt (White and Powell, 2002; White et al., 2004; Stuck and Diener, 2018), which indicates that pyroxene-bearing metabasite represents the residue after the extraction of anatectic melt as well as any residual melt that may have been left in the system prior to cooling through an elevated solidus. Finally, extensive retrogression generating amphibolite-facies overprinting on earlier granulite-facies assemblages also occurs in the Akia Terrane (Garde, 1990) and to its south (McGregor and Friend, 1992, 1997).

2.3. Sample descriptions and petrography

Orthopyroxene-bearing metabasite was examined from the Maniitsoq region. Representative samples are described below. Here, leucosome refer to the light-coloured material in outcrop that is dominated by plagioclase and quartz with minor amounts of pyroxene, and is interpreted to represent a combination of former melt, peritectic minerals and any entrained components. It is unlikely that the
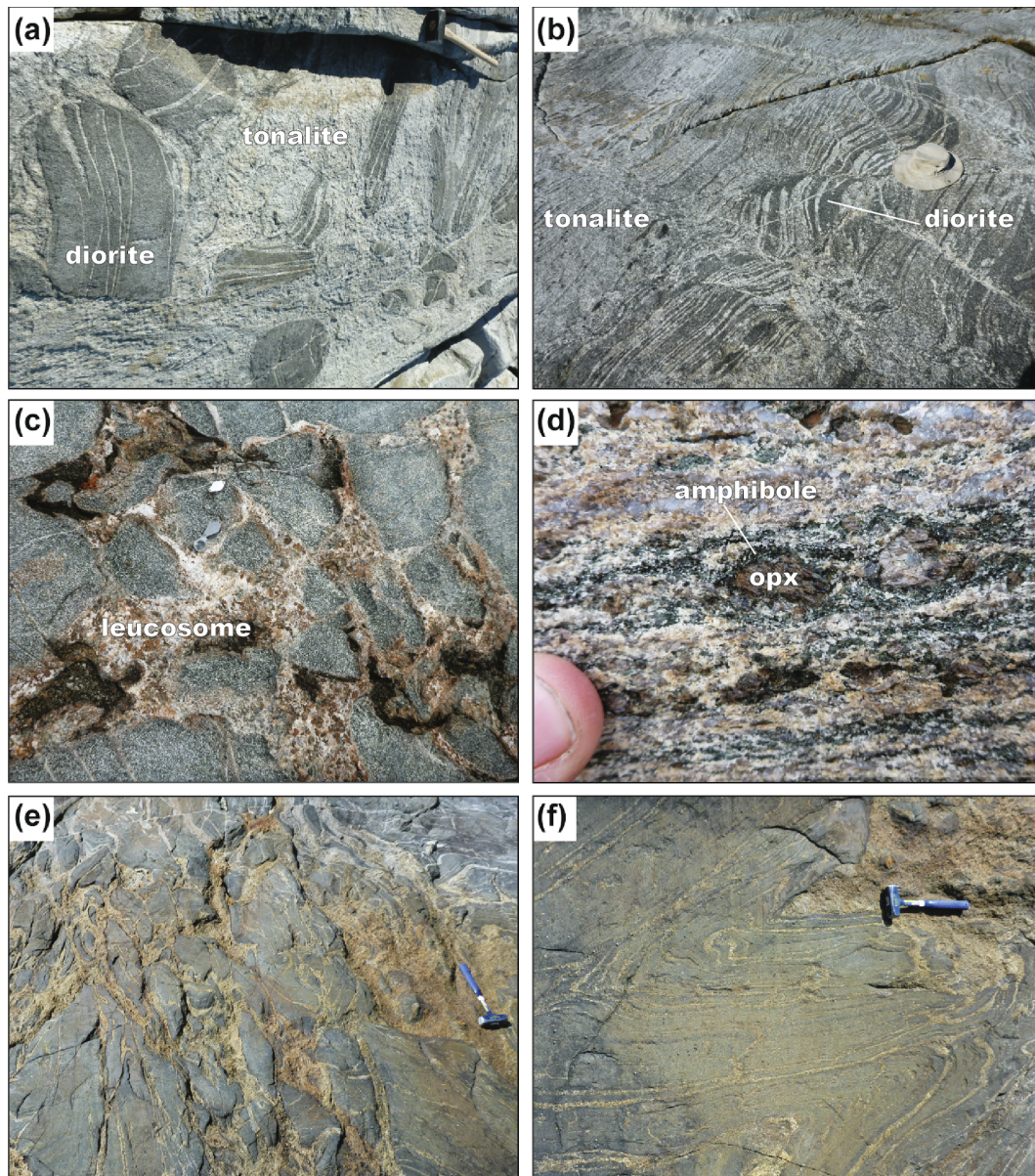
Fig. 2. Field pictures of structures and rock types from the Maniitsoq region. (a) Diorite represents the oldest exposed unit and are spatially associated with metabasite. (b) Diorite intruded by tonalite. (c) Agmatic morphology of leucosome in migmatitic metabasite. (d) Two-pyroxene leucosome with amphibole rims aligned parallel with the gneissic fabric. (e) Elongate restitic metabasite blocks. (f) Isoclinally folded metabasite blocks.

leucosome represents unmodified melt compositions due to processes associated with melt generation, segregation and extraction in migmatites (e.g. Sawyer, 1987; Brown et al., 1995; Brown et al., 2016; Yakymchuk, 2019). We refer to the darker-coloured portion of the outcrop as melanosome, which contains proportionally more ferromagnesian minerals than the leucosome. Melanosome may represent the residue of partial melting after melt extraction, especially when spatially associated with leucosome, or be refractory material that did not melt. Samples of melanosome in this study are spatially associated with and have diffuse boundaries with pyroxene-bearing leucosome; these samples are interpreted to represent residual material after melt extraction. Accessory minerals include zircon, apatite and ilmenite; rutile is absent from the investigated samples.

Sample 725 (64.99026°N, −52.1488°W) is from the melanosome of a metabasite enclave. The outcrop contains patchy orthopyroxene- and clinopyroxene-bearing leucosome in a finer-grained equigranular melanosome (Fig. 3a). The leucosome is dominated by plagioclase with cm-scale, randomly oriented porphyroblasts of euhedral orthopyroxene and clinopyroxene (Fig. 3b). The melanosome contains ~80 vol% amphibole with minor amounts of plagioclase, orthopyroxene and biotite (Fig. 4a). Orthopyroxene contains small inclusions of biotite, but biotite is also present in the matrix and has sharp grain boundaries with orthopyroxene and amphibole, which suggests that it is part of the same metamorphic assemblage. Clinopyroxene was not observed in the melanosome, but was observed in leucosome in outcrop and is inferred to be part of the peak metamorphic assemblage. Therefore, the interpreted peak metamorphic assemblage of this sample includes amphibole, plagioclase, biotite, orthopyroxene and clinopyroxene.

Sample 304 is from the base of Finnefjeld mountain (65.26859°N, −52.16566°W) and contains a network of orthopyroxene-bearing leucosome (Fig. 3e, f). The leucosome contains plagioclase, clinopyroxene and orthopyroxene (Fig. 4b) whereas the melanosome contains amphibole, plagioclase, rare quartz and accessory ilmenite and titanite. Considering the assemblages in both the melanosome and leucosome, the peak metamorphic assemblage for this sample is interpreted to be amphibole, quartz, plagioclase, clinopyroxene and orthopyroxene.
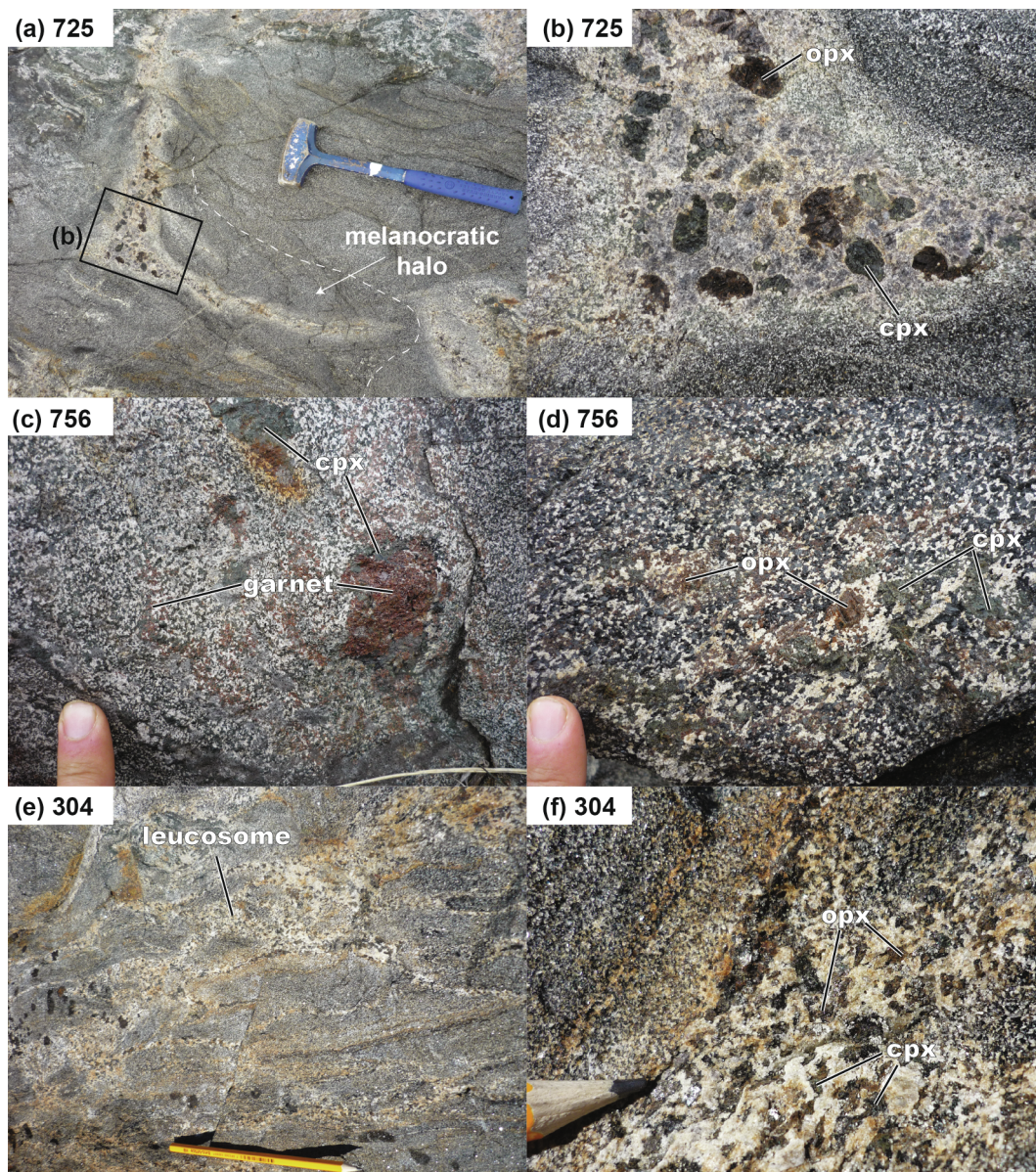
Fig. 3. Field relationships of metabasite from the Maniitsoq region. (a) Patchy leucosome surrounded by a melanocratic halo. Sample 725 was collected in the melanosome away from this halo. (b) Coarse-grained euhedral orthopyroxene and clinopyroxene in leucosome. (c) Garnet and clinopyroxene in metabasite. (d) Clinopyroxene and orthopyroxene in leucosome and location of sample 756. (e) Irregular leucosome network in a metabasite. (f) Coarse-grained peritectic orthopyroxene and clinopyroxene in the leucosome indicative of in situ partial melting.

Sample 756 is from Imartorngup Timaa (65.4414°N, −52.58055°W) and contains rare centimetre-scale garnet in melanosome in outcrop (Fig. 3c) that we were not able to sample. The same unit contains patchy orthopyroxene- and clinopyroxene-bearing leucosome with much less amphibole than the melanosome (Fig. 3d). The melanosome contains an idioblastic to subidioblastic assemblage of amphibole, plagioclase, orthopyroxene, clinopyroxene and rare quartz (Fig. 4c, d) that is inferred to be the peak metamorphic assemblage. Garnet may be part of the peak metamorphic assemblage in the same outcrop, but it is not clear if this was controlled by local bulk composition heterogeneity.

Sample 309 is from just west of Portusoq island (65.2433°N, −52.370278°W) and is a migmatitic amphibolitic gneiss that is re-folded in decimeter scale isoclinal folds. Leucosome within the gneiss are pyroxene bearing and a later generation of granitoid dykes, pods and sheets cut an earlier foliation within this rock. The melanosome is dominated by a framework of amphibole (~70 vol%) with isolated subidioblastic to xenoblastic plagioclase (~20 vol%) and quartz

(~10 vol%) (Fig. 4e, f) as well as trace amounts of calcite. Xenoblastic quartz in the melanosome has low dihedral angles between amphibole and plagioclase that are interpreted as pseudomorphs after anatectic melt (e.g. Sawyer, 1999; Holness and Sawyer, 2008). The leucosome contains clinopyroxene, orthopyroxene and amphibole as well as blocky plagioclase and rare quartz (Fig. 4e). The interface between leucosome and melanosome is sometimes slightly enriched in amphibole relative to other portions of the sample (Fig. 4e).

Samples 741 and 740 (65.47126°N, −53.07131°W) are from the same outcrop on west Maniitsoq Island (Fig. 1). The outcrop contains a metabasite with orthopyroxene-bearing leucosome. The melanosome has a granoblastic texture and contains orthopyroxene, clinopyroxene, amphibole, plagioclase and ilmenite (Fig. 4d); this is interpreted to represent the peak metamorphic assemblage. The leucosome contains a framework of coarse-grained orthopyroxene and blocky plagioclase. Quartz interstitial to plagioclase is xenoblastic and rounded quartz occurs in blocky plagioclase (Fig. 4g). Thin quartz films separating
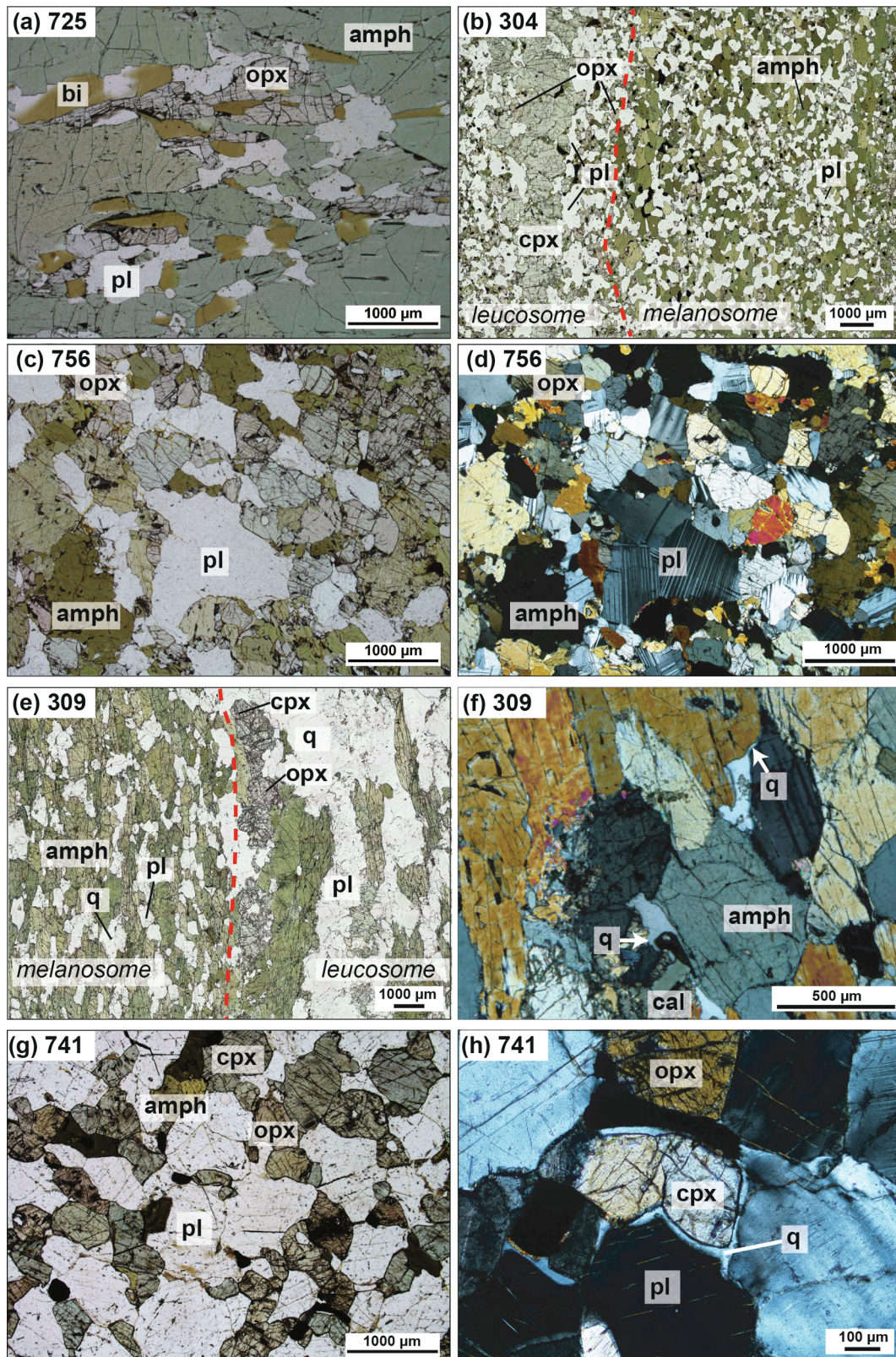
Fig. 4. Petrology of metabasite. (a) Plagioclase- and orthopyroxene-bearing assemblage in sample 725 from the melanosome in Fig. 3b. (b) Two-pyroxene lecosome in an amphibole and biotite rich matrix. (c) Inferred peak metamorphic assemblage of plagioclase, amphibole, orthopyroxene in sample 756. (d) Crossed-polarized light image of (c) for sample 756. (e) Pyroxene–amphibole–plagioclase matrix with a clinopyroxene-rich leucosome in sample 309. (f) Quartz films with low dihedral angles in sample 309 interpreted as former remnants of partial melt. (g) Granoblastic two-pyroxene assemblage of sample 741 with rare amphibole. (f) Quartz films with low dihedral angles separating clinopyroxene from plagioclase interpreted as a melt pseudomorph.

plagioclase from pyroxene with low dihedral angles are interpreted to represent pseudomorphs after anatectic melt (Fig. 4h).

Sample 202 from near Seqi (65.00960°N, −51.67560°W) is a pegmatitic orthopyroxene–clinopyroxene leucosome in a metagabbro. The anastomosing leucosome cuts across a weak foliation defined by aligned amphibole in the host metagabbro.

The above observations at the outcrop and thin section scale are consistent with partial melting of the melanosome by a continuous reaction that consumes amphibole and quartz to produce anatectic melt and peritectic pyroxene, a common reaction in granulite-facies metabasite (Hartel and Pattison, 1996; Palin et al., 2016a, b). The presence of amphibole, plagioclase and minor quartz in the melanosome indicate that the reaction did not completely exhaust the reactants and, thus, a relatively limited volume of melt was produced.

3. Methods

3.1. Geochronology

Zircon U–Pb geochronology was performed on three samples of two-pyroxene leucosome in metabasite (samples 202, 309 and 740) from the Maniitsoq region in order to determine the timing of partial melt crystallization. The U–Pb data are reported in electronic Supplementary Table S1. Zircon crystals were separated from each sample using magnetic and density techniques. These zircons, together with zircon reference standards, were cast in epoxy mounts, which were then polished to approximately half of the grain thickness for analysis. Each mount was documented with transmitted and reflected light micrographs and cathodoluminescence (CL) images prior to analysis. CL imaging used a Tescan Mira 3 VP-FESEM scanning electron microscope with Tescan panchromatic CL detector (185–850 nm spectral range) at 10 kV accelerating voltage and 16.5 mm working distance.

Zircon mineral fractions for samples 309 and 704 were analysed using secondary ionization mass spectrometry (SIMS) at the John de Laeter Centre, Curtin University, using a SHRIMP II ion microprobe. U–Th–Pb ratios and absolute abundances were determined relative to CUYZ reference zircon ($^{238}U/^{206}Pb$ age 568.55 Ma; $^{207}Pb/^{206}Pb$ age 569.49 Ma; U = 582.7 ppm; Th = 82.7 ppm; Tedeschi et al., 2019; Mole et al., 2018; A. Kennedy, John de Laeter Centre), analyses of which were interspersed with those of unknown zircon. Fractionation of $^{207}Pb^*/^{206}Pb^*$ (Pb* = radiogenic Pb) was monitored during each session by analysis of the 3465 Ma OG1 zircon standard (Stern et al., 2009) and no $^{207}Pb/^{206}Pb$ fractionation correction was deemed necessary. Measured compositions were corrected for common Pb using nonradiogenic ^{204}Pb for all SIMS analyses, as per the method implemented in the data reduction software (SQUID; Ludwig, 2009). Prior to analysis, each site was cleaned by rastering the primary ion beam over the area for up to three minutes. In most cases, corrections are sufficiently small to be insensitive to both the choice of common Pb composition and the application of a correction. ^{204}Pb correction used an average crustal composition (Stacey and Kramers, 1975) appropriate to the inferred age of the mineral. External spot-to-spot (reproducibility) uncertainties of < 1.0% (1σ) and $^{238}U/^{206}Pb^*$ calibration uncertainties of < 0.6% (1σ) were achieved in this work, as estimated by repeated measurement of the primary reference material. Calibration uncertainties are propagated by quadratic addition of the quoted uncertainties of $^{238}U/^{206}Pb^*$ ratios and dates listed in Supplementary data Table S1. Data were reduced using SQUID, in-house macros, and Isoplot (Ludwig, 2003, 2009), using decay constants of Steiger and Jäger (1977). Calculated mean ages are quoted in the text with 95% uncertainties (tσ√MSWD; Ludwig, 2003), unless specifically stated otherwise, and the value of the mean square of weighted deviates (MSWD) is also cited.

Zircon from sample 202 was analysed by LA-ICPMS, at the GeoHistory Facility, John de Laeter Centre, Curtin University. Targeted portions of individual zircon grains were ablated using a Resonetics M-

50 193 nm ArF excimer laser ablation system. Following two pre-ablation cleaning pulses spots were ablated for 35 s at a 10 Hz repetition rate using a 50 μm beam and laser energy at the sample surface of 2.3 J/cm². An additional 40 s of baseline was collected after ablation. The sample cell was flushed with ultrahigh purity He (300 mL/min) and N (1.0 mL/min). Isotopic intensities were measured using an Agilent 7700 s quadrupole ICPMS with high-purity Ar as the carrier gas. Most elements were measured for 0.01 s with the exception of ^{204}Pb, ^{206}Pb, ^{207}Pb, ^{208}Pb at 0.03 s, ^{232}Th at 0.0125 s and ^{238}U at 0.0125 s. Reference materials were run after 10 unknowns with OG1 (3465 Ma; Stern et al., 2009) used as a primary standard as it has an ablation response similar to the Archean unknown grains of interest in this work. Secondary standards GJ1 (601.7 ± 1.4 Ma; Jackson et al., 2004), Mud Tank (732 ± 5 Ma; Black and Gulson, 1978); and R33 (419.26 ± 0.39 Ma; Black et al., 2004) were employed to verify the procedure. No common-Pb correction is applied due to low ^{204}Pb counts and difficulties to obtain accurate ^{204}Pb measurements. Data reduction used the U/Pb Geochronology3 data reduction scheme in Iolite (Paton et al., 2011) and in-house Microsoft Excel macros. The weighted mean $^{238}U/^{206}Pb$ ages determined for secondary standards treated as unknowns and reduced using appropriate standards were: GJ1 604 ± 5 Ma (n = 15; MSWD = 0.37), Mud Tank 736 ± 10 (n = 16; MSWD = 0.45), and R33 419 ± 4 (n = 15; MSWD = 0.63), consistent with the recommended values. Ages include internal and external sources of uncertainty propagated in quadrature.

3.2. Geochemistry

Bulk rock compositions were determined at ALS Laboratories (Ireland) using the ME-ICP06 analytical package. Samples were digested after lithium metaborate fusion and major element concentrations were determined by ICP-AES and trace elements by ICP-MS. The ratio of ferric to ferrous iron was determined by titration (package Fe-VOL05) at ALS Laboratories. Results are presented in Supplementary Table S2.

3.3. Phase equilibrium modelling

Phase equilibrium modelling was used to determine the *P–T* conditions of Mesoarchean metamorphism in the Maniitsoq region of the Akia Terrane. Melanosome of the four metabasite samples that host orthopyroxene-bearing leucosome were selected for modelling based on the range of SiO_2 and MgO concentrations (Fig. 5a) and spectrum of chondrite-normalized rare earth element (REE) patterns (Fig. 5b) of mafic rocks in the Akia terrane. Metamorphic assemblages were modelled in the NCKFMASHTO (Na_2O–CaO–K_2O–FeO–MgO–Al_2O_3–SiO_2–H_2O–TiO_2–O) chemical system using the activity-composition models from Green et al. (2016), the internally consistent thermodynamic database (ds62) of Holland and Powell (2011) and the THERMOCALC software package (Powell and Holland, 1988). Pure phases considered in our modelling include quartz, rutile, sphene, and aqueous fluid (H_2O). Mineral abbreviations are from Holland and Powell (2011).

Modelling anatectic systems requires an estimate of the amount of H_2O and oxidation state (i.e. Fe^{3+} versus Fe^{2+}) of the system. Suprasolidus rocks are generally not considered to have excess H_2O as the very small amount of free H_2O at the solidus is partitioned into anatectic melt (e.g. Clemens and Vielzeuf, 1987) and the preservation of high-temperature assemblages requires that melt was extracted from the system during prograde metamorphism (e.g. White et al., 2005). At crustal conditions, along the solidus, the solubility of H_2O in anatectic melt increases with pressure (e.g. Palin et al., 2016a). Therefore, for phase equilibrium modelling of suprasolidus rocks, the amount of H_2O in the bulk composition must be set such that there was no excess fluid in the system. Temperature–composition (*T–X*) diagrams were constructed at 0.5 GPa to constrain the appropriate amount of H_2O in each
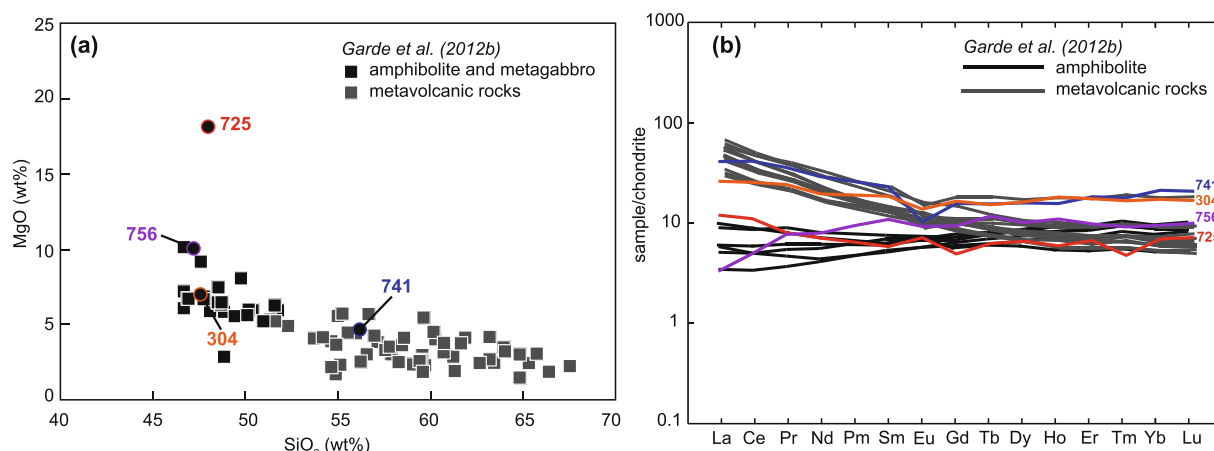
Fig. 5. (a) Whole rock MgO versus SiO_2 (wt%) for metabasite samples modelled here compared with metabasite compositions from Garde et al. (2012b) for the Maniitsoq region. (b) Chondrite-normalized rare-earth element profiles of four metabasite samples compared with the metabasite and metavolcanics rocks from the Akia Terrane (Garde et al., 2012b). Chondrite values are from McDonough and Sun (1995).

Table 1
Compositions used in phase equilibrium modelling.

| | | | wt% | | | | | | | | | | | | |
Sample	Latitude	Longitude	SiO_2	TiO_2	Al_2O_3	Fe_2O_3	FeO	MnO	MgO	CaO	Na_2O	K_2O	P_2O_5	LOI	Total
304	65.44140	−52.58055	47.60	0.79	14.95	3.66	9.30	0.24	6.93	10.75	2.69	0.43	0.06	0.41	97.81
725	64.99026	−52.14880	48.00	0.35	10.65	2.01	7.95	0.18	18.05	8.57	1.62	1.01	0.03	0.79	99.21
741	65.47126	−53.07131	56.20	0.55	13.95	2.55	9.45	0.21	4.63	9.04	2.63	0.47	0.07	< 0.01	99.75
756	65.44140	−52.58055	47.20	0.60	15.85	2.18	8.70	0.19	9.99	12.75	1.39	0.13	0.03	0.40	99.41

| | | | mol% | | | | | | | | | | | | |
Sample	Figures		H_2O	SiO_2	Al_2O_3	CaO	MgO	FeO	K_2O	Na_2O	TiO_2	O	$Fe^{3+}/[Fe^{2+} + Fe^{3+}]$		Total
304	6c, 7c		3.14	49.24	9.11	11.91	10.69	10.90	0.28	2.70	0.62	1.43	0.26		100.00
725	6a, 7a		6.77	43.97	5.75	8.41	24.65	7.48	0.59	1.44	0.24	0.69	0.19		100.00
741	6d, 7d		2.46	57.68	8.44	9.94	7.08	10.08	0.31	2.62	0.42	0.98	0.20		100.00
756	6b, 7b		4.15	46.78	9.26	13.54	14.76	8.84	0.08	1.34	0.45	0.81	0.18		100.00

sample. Using the T–X diagrams, the amount of H_2O in the system was chosen to just stabilize the interpreted peak metamorphic assemblage at the solidus at 0.5 GPa. High-temperature metamorphic assemblages are also sensitive to the oxidation state of the system and the ratio of ferric to ferrous iron in the system affects the stability of oxides and major silicate minerals (e.g. Diener and Powell, 2010). Consequently, we use the values of ferric and ferrous iron measured by ICP-OES and titration. All modelled compositions are specified in Table 1.

Trace element modelling was also conducted to determine the equilibrium concentration of trace elements in anatectic melt at a range of P–T conditions near the estimated peak of metamorphism. The methodology used here is similar to that applied in previous studies and combines the output of phase equilibrium modelling with mineral–melt partitioning expressions for trace elements (Nagel et al., 2012; Yakymchuk and Brown, 2019; Janousek and Moyen, 2019). Briefly, melt and mineral weight fractions were calculated from the THERMOCALC output and combined with partition coefficients for mafic rocks from the compilation of Bédard (2006). Using the batch melting expression of Hanson (1978) and the whole-rock concentrations determined from ICP-MS, the concentrations of rare earth elements in the model melt were calculated from 0.4 to 1.0 GPa at 900 °C at 0.1 GPa intervals. Modelled melt compositions were then compared with published compositions of tonalites from the Maniitsoq region (Gardiner et al., 2019).

Several important assumptions must be made to apply the results of phase equilibrium modelling to the trace element compositions of tonalites from Maniitsoq. First, we assume that the preserved high-temperature metamorphic assemblage in the metabasite was similar to that of the residue when melt was extracted. Second, we assume that the measured trace element composition of the residue was similar to that when the melt was extracted and that melt extraction occurred as a single pulse (c.f. Yakymchuk and Brown, 2014a). Considering that the fertility of these rocks is expected to be fairly limited (< 20 vol% melt) at the exposed crustal level, the assumption that the trace element composition of the residue is similar to that of the protolith is considered a reasonable approximation. Third, we do not consider the accessory minerals to contribute to the trace element composition of the melt. The low concentrations of Zr (< 100 ppm) and P_2O_5 (< 0.10 wt %) in the measured compositions (Supplementary Table S2) imply that the modes of zircon and apatite are very low and their absence from the modelling is not expected to substantially change the composition of the modelled melt. Low modes of zircon are also expected due to Zr accommodation in amphibole (e.g. Bea et al., 2006), which is part of the metamorphic assemblage for the four investigated metabasite samples. Finally, the composition of the magma extracted from the source will likely be a combination of melt and entrained minerals or residue (e.g. Stevens et al., 2007; Clemens et al., 2011) – the entrainment of these components is not considered in the modelling here when comparing the modelled melt compositions to measured compositions of tonalite in the Maniitsoq region. Although the assumptions listed above will have subtle effects on the modelled melt compositions versus the composition of tonalite, the modelling provides a first-order test of the genetic link between the tonalite and the granulite-facies mafic rocks that builds on existing Hf isotope evidence (Gardiner et al., 2019).

4. Results

4.1. Geochemistry

The compositions of the metabasite samples investigated here are compared with the compositions of mafic rocks from the Akia Terrane (Garde et al., 2012b) in Fig. 5. Sample 725 contains 17 wt% MgO (Fig. 5a), the highest of the samples investigated in detail, and has a flat chondrite-normalized rare earth element pattern and the lowest concentrations of the REE of the investigated samples (Fig. 5b). Sample 756 has a moderate concentration of MgO (10 wt%), low SiO_2 (~47 wt%) and is slightly depleted in the LREE compared with the HREE (Fig. 5). Sample 304 has ~ 6 wt% MgO, ~47 wt% SiO_2 and a flat chondrite-normalized REE pattern (Fig. 5). Sample 741 has the lowest MgO (~5 wt%) and highest SiO_2 (~56 wt%) of the four samples. It is slightly enriched in the LREE compared with the HREE and contains a pronounced negative Eu anomaly (Fig. 5b).

Compared with the compilation of unaltered rocks of Garde et al. (2012b), samples 756 and 304 plot near the values for their amphibolite (Fig. 5). Sample 741 plots among their metavolcanic rocks and 725 plots at much higher MgO values than their amphibolite for a similar SiO_2 content (Fig. 5a). Samples 725 and 756 have similar chondrite-normalised profiles to the amphibolite of Garde et al. (2012b) (Fig. 5b). Samples 304 and 741 have similar chondrite-normalized profiles to the most LREE-enriched metavolcanic rocks from Garde et al. (2012b), but have higher concentrations of the HREE (Fig. 5b). In general, the four samples investigated here are considered broadly representative of the range of compositions of amphibolite and mafic metavolcanic rocks observed in the Akia Terrane.

4.2. Phase equilibrium modelling

4.2.1. Pressure–temperature estimates

The results of phase equilibrium modelling of four orthopyroxene-bearing samples are shown in Fig. 6. All modelled metamorphic assemblages shown in Fig. 6 include the presence of anatectic melt. Subsolidus phase assemblages were not calculated due to the uncertainty of the prograde *P–T* path that is required for a melt re-integration calculation to retrieve the protolith composition (e.g. Bartoli, 2017).

For sample 725, plagioclase is predicted at < 760 ˚C and clinopyroxene is restricted to > 900 ˚C (Fig. 6a). The presence of plagioclase and absence of clinopyroxene (Fig. 4a) in sample 725 is not compatible with a single modelled stability field in Fig. 6a. However, the mineral assemblages throughout the outcrop are heterogeneous. The bulk sample used to calculate the phase diagram was taken from the melanosome and away from pyroxene-bearing leucosome and does not contain clinopyroxene. A narrow melanocratic halo between the clinopyroxene-bearing leucosome and the melanosome (Fig. 3a) suggests that plagioclase was locally consumed to produce the clinopyroxene-bearing leucosome. Therefore, the peak metamorphic temperatures may have reached > 900 ˚C as indicated by the presence of peritectic clinopyroxene in leucosome in outcrop and local depletion of plagioclase in the melanosome immediately surrounding the leucosome. At ~850–900 ˚C and 6 kbar, the modelling predicts ~75–80 one-oxide normalized mol.% (~equivalent to vol.%) hornblende, which is broadly consistent with the amount of amphibole observed in thin section (Fig. 4a). Nonetheless, the modelling does not predict that plagioclase is stable at these conditions, which contrasts with the observation of plagioclase in thin section (Fig. 4a). Garnet is predicted to be stable at *P* > 1.4 GPa at these temperatures and is not observed in outcrop. Phase equilibrium modelling also predicts the presence of biotite at ultra-high temperature (> 900 ˚C) conditions. This may be due to the absence of quartz and plagioclase in the modelling at high temperatures, which are necessary reactants in fluid-absent incongruent biotite-breakdown melting reactions (e.g. Patiño Douce and Beard, 1995).

Therefore, the modelled peak *P–T* conditions are restricted to > 900 ˚C and < 1.4 GPa, which equates to an apparent thermal gradient of > 650 ˚C/GPa. However, these *P–T* estimates should be treated with caution given the outcrop-scale heterogeneity and the inconsistency between the modelled phase assemblages and the observed mineral assemblages.

Sample 756 contains an interpreted peak assemblage of orthopyroxene, clinopyroxene and rare garnet. Garnet was only observed in outcrop and not in thin section. Without garnet, the peak metamorphic assemblage is restricted to > 800 ˚C and < 0.8 GPa (Fig. 6b). With garnet and orthopyroxene, the assemblage is restricted to 0.8–1.0 GPa at 850 to > 1000 ˚C (Fig. 6b). Both assemblages are consistent with an apparent thermal gradient of > 1050 ˚C/GPa.

Sample 304 contains an interpreted peak assemblage that includes orthopyroxene and clinopyroxene without garnet. This assemblage is restricted to < 0.8 GPa and > 770 ˚C to > 850 ˚C with increasing pressure (Fig. 6c). Given the strong sensitivity of magnetite stability to the amount of Fe^{3+} in the modelled system and the possibility of oxidation due to sample processing (e.g. Diener and Powell, 2010), it is unclear if magnetite was part of the peak metamorphic assemblage (Fig. 6c). In addition, there is some uncertainty in how robust the activity–composition models for augite and amphibole are regarding site mixing of Al and Fe^{3+} (e.g. Forshaw et al., 2019). Nonetheless, the estimated *P–T* conditions equate to an apparent thermal gradient of > 1050 ˚C/GPa.

For sample 741, the predicted stability field of orthopyroxene is restricted to > 730 ˚C at 0.2 GPa and > 850 ˚C at 0.7 GPa (Fig. 6d). Garnet is predicted to be stable at > 0.75 GPa at these temperatures, but is absent from the sample. Amphibole is present in the sample, which restricts peak temperatures to < 870 ˚C. However, amphibole only represents < 5 vol% of the sample and its preservation may be due to local bulk compositional control (i.e. local volumes with higher a_{H2O}); hence this sample may have reached temperatures higher than the hornblende-out phase boundary in Fig. 6d. Nonetheless, the predicted *P–T* conditions represent an apparent thermal gradient of > 1050 ˚C/GPa

In summary, the investigated samples all contain orthopyroxene-bearing metamorphic assemblages that are consistent with suprasolidus conditions at pressures of < 0.9 GPa and temperatures ≫750 ˚C across the Maniitsoq region of the Akia Terrane. With the exception of sample 725, which is a compositional outlier (Fig. 5a) and has a modelled wide range of possible pressures at peak temperatures (Fig. 6a), the remaining samples all record minimum apparent thermal gradients of > 1050 ˚C/GPa. The presence of peritectic clinopyroxene in sample 725 suggests that temperatures may have locally exceeded 900 ˚C (Fig. 6a) in parts of the Maniitsoq region, although the results from this sample need to be treated with caution given the outcrop-scale heterogeneity in *P–T*-sensitive mineral assemblages (Fig. 3a).

4.2.2. Trace element modelling

Chondrite-normalized REE profiles for modelled melt compositions for 0.4–1.0 GPa at 900 ˚C of each of the four modelled compositions is shown in Fig. 7. Also shown in Fig. 7 for comparison are the range of REE profiles measured in c. 3.0 Ga tonalite from Gardiner et al. (2019). As a group, 3.0 Ga tonalite have negatively sloping REE profiles, typical of the TTG series (e.g. Moyen and Martin, 2012), with minor negative to strong positive Eu anomalies (Fig. 7).

For sample 725, all melt compositions from 0.4 to 1.0 GPa are approximately the same and are depleted in LREE relative to tonalite. Middle and heavy REE plot in the field of the tonalities in Fig. 7a, but concentrations of the LREE in the model melts are lower than measured compositions.

For sample 756, all modelled melt compositions have lower La, Ce, Pr and Eu than tonalite and have HREE concentrations that plot within the field of the tonalite with the exception of Lu for the 0.4–0.8 GPa model melts (Fig. 7b). However, model melt from a garnet-present
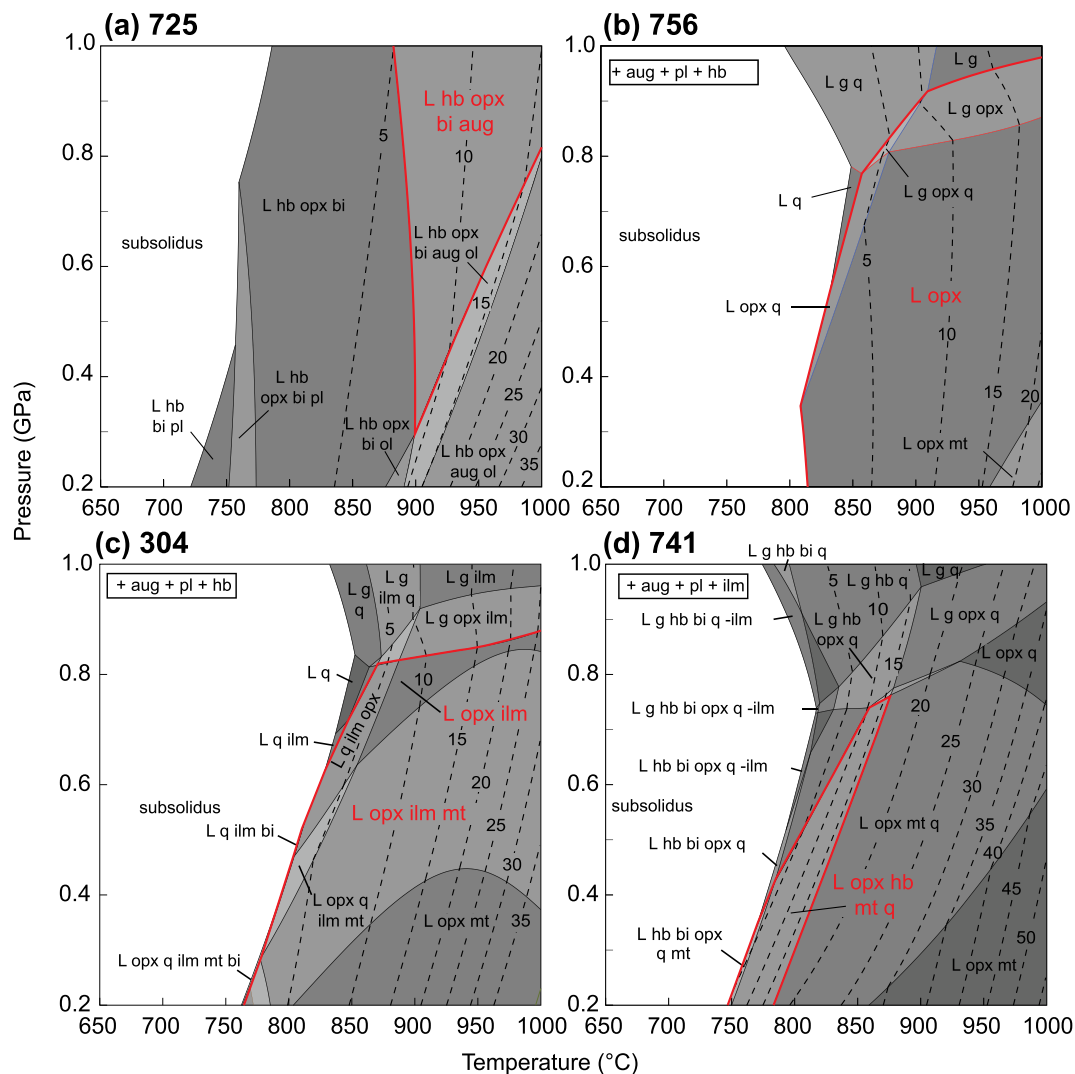
Fig. 6. Pressure–temperature isochemical phase diagrams for four metabasite samples from the Maniitsoq region of the Akia Terrane. The inferred peak metamorphic assemblage is outlined by a red line. Dashed lines represent the one-oxide normalized molar percentage of melt in the system, which is approximately equivalent to vol%. (For interpretation of the references to colour in this figure legend, the reader is referred to the web version of this article.)

assemblage (0.9 and 1.0 GPa) have predicted HREE concentrations that plot in the range of tonalite (Fig. 7b).

For sample 304, model melt compositions from 0.4 to 0.8 GPa (with orthopyroxene but no garnet in the source) have slightly enriched LREE that plot in the range of tonalite values, but also have flat HREE that are more enriched than measured tonalite compositions (Fig. 7c). Melt compositions at 0.9 and 1.0 GPa (which includes garnet in the source) are more depleted in the HREE and fall in the range of measured to-nalite compositions (Fig. 7c). These modelled melt composition provide the best match to the measured compositions of tonalite in the Man-iitsoq region.

For sample 741, modelled melt compositions are all enriched in Pr, Nd and Sm relative to the tonalite compositions and have moderate to strong Eu anomalies. Melt compositions calculated at 0.4–0.8 GPa are more enriched in the HREE than tonalite (Fig. 7d). When garnet is in the residue at 0.9 and 1.0 GPa, the HREE are depleted and model melt compositions plot within the field defined by tonalite (Fig. 7d).

In summary, with the exception of sample 756, which may have garnet in the peak assemblage, the modelled melt compositions in the other three samples at peak *P–T* conditions do not produce the appro-priate low concentrations of the HREE in tonalite from the Maniitsoq region. However, extrapolation from the estimated peak metamorphic conditions into the garnet stability field by 0.1–0.2 GPa from the

estimated pressures of peak metamorphism generates model composi-tions that are generally compatible with measured tonalite composi-tions.

5. U–Pb geochronology

5.1. 309 – two-pyroxene leucosome

Zircon crystals are subhedral to euhedral and have moderate to high aspect ratios (1:3 to 1:5). In CL images the grains display oscillatory zoned cores overgrown and partially resorbed by dark-CL response rims (high U) which in turn are overgrown by bright-CL response rims (low U) (Fig. 8a). One analysis is greater than 10% discordant and one analysis which failed to yield U/Pb ratios (Group D) are not considered further. Fourteen analyses (Group P) on high uranium overgrowths and lower uranium core domains yield $^{207}Pb*/^{206}Pb*$ ages of 3026–2988 Ma (Fig. 8a), are interpreted to reflect either prolonged metamorphic growth or the partial retention of the isotopic signature from dissolved inherited cores and new zircon growth. The youngest statistically coherent component of this group yields a weighted mean $^{207}Pb*/^{206}Pb*$ age of 2989 ± 5 Ma (MSWD 0.68, n = 4), which is interpreted as dating one period of high-temperature metamorphism and leucosome crystallization. No correlation is apparent between U
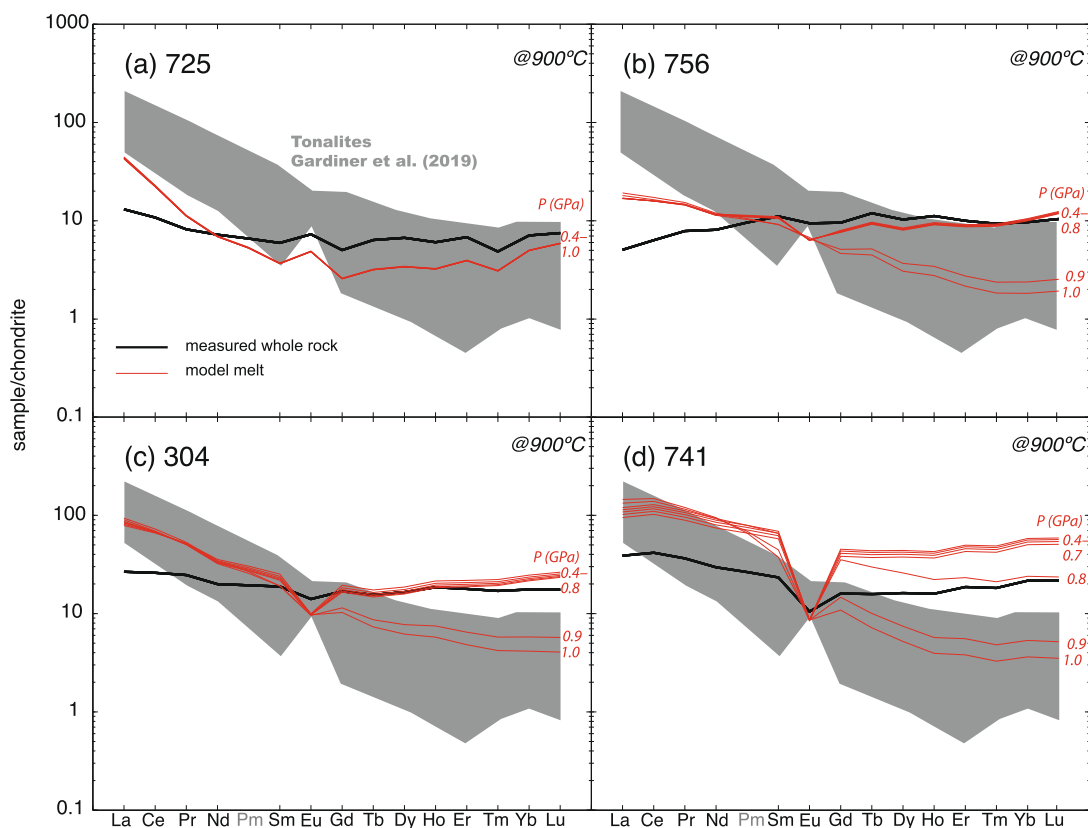
Fig. 7. Modelled chondrite-normalized rare earth element profiles of melt in equilibrium with the metamorphic assemblages in Fig. 6 at 900 °C and for a variety of pressures. The grey fields are the range of tonalite orthogneiss compositions from Gardiner et al. (2019). Except for sample 725, all other modelled melt compositions are most consistent with the tonalite compositions at pressures of 0.9 and 1.0 Ga. For sample 725, the modelled compositions from 0.4 to 1.0 GPa overlap on the diagram.

and $^{207}Pb*/^{206}Pb*$ age, which under normal crustal conditions would be inconsistent with radiogenic-Pb mobility as the dominant influence on the age pattern observed (that is higher U would be expected to correlate with younger age). Nonetheless, at temperature conditions > 900 °C crystal structure control would be diminished as all zircon would be above their Pb blocking temperature and radiogenic-Pb mobility viable to explain the U–Pb scatter. Hence, ages of core and rims may relate to near simultaneous radiogenic-Pb mobility and growth, potentially a natural occurrence of high-grade metamorphism and leucosome development (e.g. Kirkland et al., 2018c). One low U (51 ppm) rim analysis (Group M) yields an imprecise $^{207}Pb*/^{206}Pb*$age of 2871 ± 88 Ma (1σ). While only a single analysis, and so must be interpreted with caution, this result may be interpreted as an estimate of the timing for a low-temperature metamorphic (hydrothermal) overprint on these rocks. Four analyses (Group X) of oscillatory zoned cores yield a weighted mean $^{207}Pb*/^{206}Pb*$ age of 3048 ± 5 Ma (MSWD = 1.05), interpreted as the magmatic crystallization age of the host rock now inherited into the leucosome.

5.2. 740 – Pyroxene bearing leucosome

Zircon crystals recovered from sample 740 are subhedral to euhedral and typically elongate. In CL images, oscillatory zoned partially reabsorbed cores are common, low CL response and many grains are overgrown by additional homogeneous low CL response rims (Fig. 8b). Eleven analyses (Group M) of cores and homogenous rims (including four analyses with extreme uranium content) yield a weighted mean $^{207}Pb*/^{206}Pb*$ age of 3009 ± 3 Ma (MSWD = 1.9), interpreted as the age of high-grade metamorphism, leucosome crystallization and isotopic resetting of protolith zircon. Six analyses (Group P) of both rims

and cores yield $^{207}Pb*/^{206}Pb*$ ages of 2993–2914 Ma (Fig. 8d), and are interpreted to have lost radiogenic-Pb consistent with their Tera–Wasserberg discordant character.

5.3. 202 – Orthopyroxene-clinopyroxene leucosome in gabbroic gneiss

The zircon crystals are euhedral and under CL display well-developed idiomorphic zoning with occasional dissolution fronts. Three analyses (Group D) are > 5% discordant (Fig. 8c) and are interpreted to have been influenced by radiogenic-Pb loss or common Pb. Seventeen analyses (Group I) of idiomorphically zoned zircon yield a weighted mean $^{207}Pb/^{206}Pb$ age of 3001 ± 14 Ma (MSWD = 0.2), interpreted as the magmatic crystallization age of the zircon in the leucosome, consistent with the zircon internal textures. These analyses yield moderate to high Th/U ratios of 1.4–2.5.

6. Discussion

6.1. Mesoarchean high-temperature metamorphism and anatexis

The three ages from in situ orthopyroxene-bearing leucosome (samples 202, 309 and 740) in the Maniitsoq region range from *c.* 3010 to *c.* 2990 Ma (Fig. 8a–c). These ages are broadly consistent with previously reported zircon U–Pb geochronology of the timing of granulite-facies metamorphism within the southern Akia Terrane. Garde et al. (2000) report an age of 2981 ± 8 Ma from a grey gneiss from the mouth of Fiskefjord (sample 339199; Fig. 1) as the granulite-facies thermal maximum. Friend and Nutman (1994) report an age of 2999 ± 4 Ma for the granulite-facies metamorphism of a metasedimentary rock from Nordlandet (sample VM90-18; Fig. 1). When
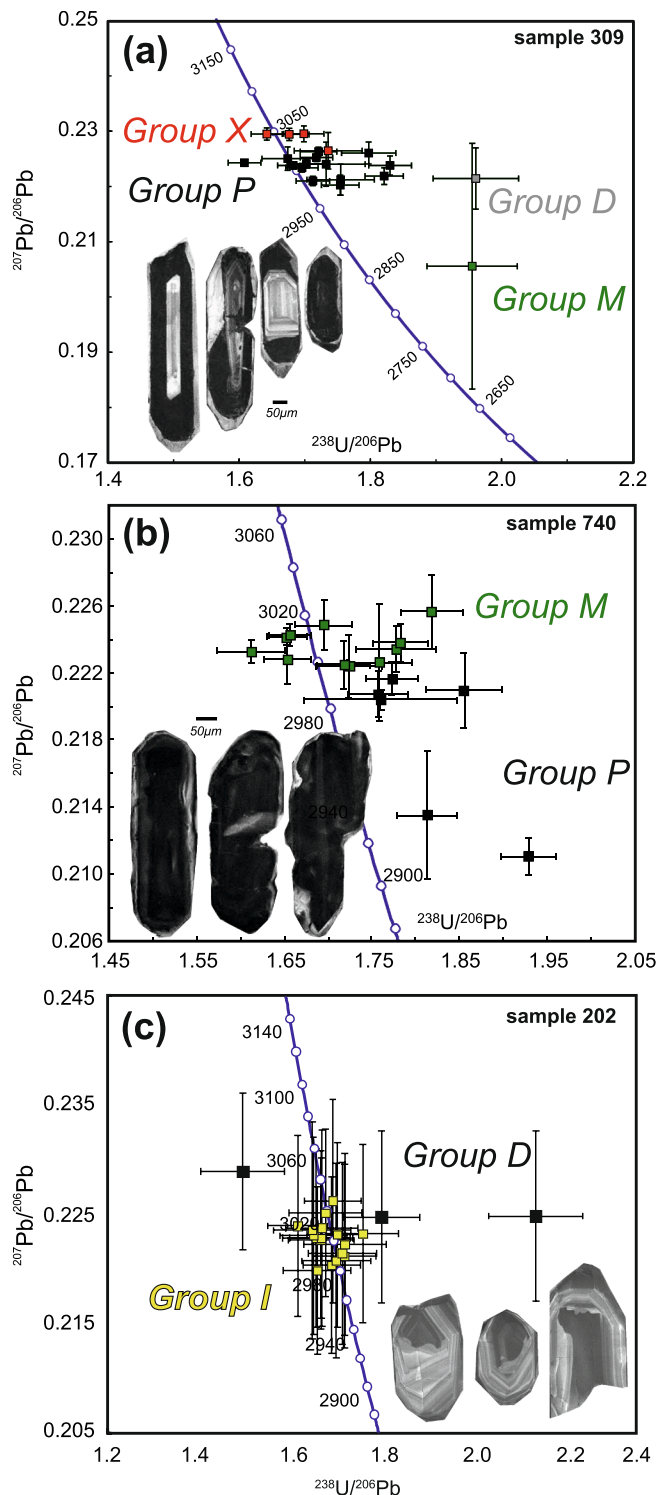
Fig. 8. U–Pb Tera-Wasserberg diagrams for three leucosome samples from the Akia Terrane. Different zircon groups are discussed in the text. D = outside discordance limits, I = idiomorphically zoned, P = radiogenic Pb loss, M = metamorphic (subsequent events appended a number), and X = xenocryst. Error bars are shown at 2σ.

combined with previous geochronology, the three new ages reported here are consistent with a regional granulite-facies metamorphic event that occurred from at least Maniitsoq Island in the north to Nordlandet in the south in the western portion of the Akia Terrane. The range of ages may reflect diachronous metamorphism (e.g. Garde et al., 2000) or may alternatively represent a protracted granulite-facies metamorphic

event across the Akia Terrane, which is more likely given that there is no clear spatial trend in ages (Fig. 1). Finally, these ages generally overlap the timing of tonalitic crustal growth (e.g. Gardiner et al., 2019).

The timing of zircon growth in the pyroxene-bearing leucosome relative to the *P–T* evolution has important implications for the absolute timing of the thermal maximum of the Akia terrane at c. 3.0 Ga. Zircon in anatectic systems is expected to dissolve during prograde metamorphism and partial melting and only grow when zircon saturation is reached in the melt during cooling and melt crystallization (e.g. Kelsey et al., 2008; Yakymchuk and Brown, 2014b; Kohn et al., 2015; Yakymchuk et al., 2017). Variable zircon U–Pb ages from granulite-facies terranes have been attributed to different solidus temperatures of residual rocks and zircon crystallization near the estimated solidi (e.g. Korhonen et al., 2013). The calculated solidus temperatures for the different samples investigated in this study are not considerably different (Fig. 6). Therefore, the range of zircon ages recording granulite-facies metamorphism cannot be explained by slow cooling through variable solidus temperatures. Nonetheless, the Mesoarchean thermal maximum in the Akia Terrane must have been earlier than these c. 3.0 Ga zircon U–Pb ages. Whether the thermal maximum migrated across the Akia Terrane (c.f. Garde et al., 2000) or was coeval across the terrane is not possible to evaluate with the current data set due to three reasons; (1) growth of zircon is not necessarily expected to record the timing of the thermal maximum (i.e. peak metamorphism) in high-temperature metamorphic rocks; (2) zircon growth and Pb diffusion processes may be simultaneous or diachronous and distinguishing high-grade growth versus resetting processes is inherently challenging; and (3) in contrast to neoblastic growth, radiogenic-Pb mobility may be most prevalent during the thermal maximum in a system that exceeds the zircon Pb blocking temperature (~900 °C) or in a system below this temperature in the case of fluid-induced zircon dissolution or disturbance. Our phase equilibrium modelling suggests that peak metamorphic temperatures may have locally exceeded this blocking temperature (sample 725; Fig. 6a). Despite these restrictions, it is nonetheless clear that granulite-facies metamorphism was broadly contemporaneous across the western extent of the Akia Terrane (from Maniitsoq in the north to Nordlandet in the south) at c. 3.0 Ga and may have slightly predated this if temperatures exceeded the Pb-blocking temperature in zircon.

The *P–T* conditions of peak metamorphism obtained using phase equilibrium modelling reported in this work are similar to the results of Riciputi et al. (1990) and Dymek (1984) from Nordlandet in the southern Akia Terrane, although they estimated slightly higher pressures (0.8–0.9 GPa) based on conventional thermobarometry; these estimates are probably within uncertainty of those from our phase equilibrium modelling (c.f. Palin et al., 2016c). Garde et al. (1986) report an undated orthopyroxene- and garnet-bearing agmatite in metabasite from just north of the head of Qussuk to the southwest of the Maniitsoq region (Fig. 1); this assemblage is consistent with the parageneses observed in our metabasite samples. Applying our phase equilibrium modelling, the orthopyroxene leucosome-bearing metabasic rocks suggest apparent thermal gradients at the metamorphic peak of > 1000 °C/GPa. Such elevated geothermal gradients reflect the high *dT/dP* metamorphic group of Brown and Johnson (2018) and are usually found in two tectonic environments: (1) the base of thick crustal plateaus (e.g. Jamieson and Beaumont, 2013), or (2) regions with thin lithosphere such as in back-arc settings in modern environments (e.g. Currie and Hyndman, 2006). The relatively low pressures (< 0.8 GPa) of high-temperature metamorphism in the Akia Terrane—roughly equivalent to burial depths of < 26 km assuming a crustal density of 2700 kg/m^{3}—are inconsistent with the base of substantially thickened crust. This maximum depth is also probably overestimated if the overlying material was not granitic crust. Furthermore, extrapolation along this apparent thermal gradient to 1.2 GPa (~45 km deep) equates to temperatures of ~1200 °C, which is approaching the liquidus for

crustal rocks (e.g. Gerya et al., 2008); such melt-rich rocks would be unable to mechanically support a thick crustal plateau. The estimated maximum crustal thickness of < 45 km given the apparent thermal gradients calculated from the assemblages in the metabasite in the Akia terrane (Fig. 6) is also too thin to be associated with a tectonic environment where partial melting occurs in laterally-thickened arc crust (e.g. Nagel et al., 2012). Therefore, a geodynamic setting with thin crust is the best candidate for the Akia Terrane at c. 3.0 Ga during granulite-facies metamorphism.

6.2. Geodynamic setting of the Akia Terrane in the Mesoarchean

In Archean cratons, the source of TTGs is the partial melting of hydrated metabasite (e.g. Rapp et al., 1991; Moyen and Martin, 2012; Nagel et al., 2012; Martin et al., 2014; Moyen and Laurent, 2018), but the geodynamic setting of anatexis that generates these rocks is controversial (e.g. Bédard, 2006; Johnson et al., 2014, 2017). In the Akia Terrane, c. 3.0 Ga tonalite was suggested to have been derived from partial melting of subducted oceanic crust based primarily on their trace element compositions (Winther and Newton, 1991; Garde, 1997) or melting of (older) mafic crust at variable depths that do not require a subduction origin (Gardiner et al., 2019), such as a stagnant-deformable lid regime (c.f. Sizova et al., 2015, 2018). Because each of these processes implies different depths of melting, this is an important factor in determining the geodynamic setting of tonalite generation in the Akia Terrane at 3.0 Ga.

Trace element modelling of the four metabasite in this study suggests that the depleted concentration of HREE in the melt (modelled equivalents for tonalite) cannot be reproduced by melting at the peak *P–T* conditions recorded by the samples. Although the modelling does not reproduce the very low concentrations of the HREE in some tonalite samples (Fig. 7), this may be due to several factors. First, the tonalite may be derived from slightly higher pressures (> 1.0 Ga) where garnet modes were probably higher. Importantly, however, extrapolation along an apparent thermal gradient of 1000 ˚C/GPa to 0.9 GPa and 900 ˚C (~3 km deeper) predicts garnet-bearing assemblages. These yield model melt compositions that better reproduce the measured trace element compositions of tonalitic orthogneiss (Gardiner et al., 2019). Second, because garnet stability and modal proportions are bulk-composition dependant (e.g. Moyen and Martin, 2012; Palin et al., 2016a, b; Johnson et al., 2017), our four modelled compositions may not have encompassed the complete variety of metabasite in the Akia terrane. Some compositions may have generated melt with higher proportions of garnet in the residue at < 1.0 GPa (e.g. Palin et al., 2016a), resulting in more HREE-depleted melt compositions. Finally, the fractionation of HREE-rich hornblende out of the tonalite magma during ascent or emplacement may result in depleted HREE compositions in the measured tonalite relative to the melt extracted from their sources (e.g. Reichardt and Weinberg, 2012; Liou and Guo, 2019; Yakymchuk et al., 2019). Nonetheless, our modelling suggests that partial melting of > 3.0 Ga metabasite in the Akia Terrane at crustal depths as shallow as ~30 km can generate tonalite with depleted chondrite-normalized HREE profiles found in the c. 3.0 Ga tonalite.

Partial melting at depths of ~30 km does not necessarily require melting of a subducted slab at depths exceeding the estimated thickness of the Archean crust (30–45 km for basaltic oceanic crust; Herzberg and Rudnick, 2012). In contrast, depths of ~30 km are broadly consistent with the results of numerical models of stagnant-deformable lid tectonics in an oceanic plateau environment without subduction (e.g. Sizova et al., 2018). However, our results do not preclude the possibility that some tonalite may have been derived from greater depths, possibly associated with melting of a subducted slab. However, a subduction zone is not required to explain the REE compositions of tonalite in the Maniitsoq region. Further, Gardiner et al. (2019) used Hf isotopes to show that the mafic parent to 3.0 Ga tonalite was mafic crust of some antiquity, perhaps Eoarchean or even Hadean. A stagnant lid

environment may better explain the incorporation of a component of > 800 Myr old mafic crust in the genesis of these tonalites (e.g. Gardiner et al., 2019).

6.3. Duration of Mesoarchean high temperatures

The similar ages of high-*T*–low-*P* metamorphism determined across the Akia Terrane and to its north on Maniitsoq Island suggest that this region was a coherent entity at this time. Tectonic models for the Akia Terrane include accretion of volcanic arcs to a Mesoarchean core and subsequent subduction-related magmatism (Garde et al., 2000). Recent work also speculates that this was followed by the impact of a giant bolide at ≥3000 Ma (Garde et al. 2012a, 2014; Scherstén and Garde, 2013; Keulen et al., 2015). Alternatively, the region may have been relatively stagnant or undergoing extension during the Mesoarchean followed by terrane accretion and associated metamorphism in the Neoarchean (e.g. Kirkland et al., 2018a; Friend and Nutman, 2019). We evaluate these models below by using a combination of field evidence and results of zircon geochronology.

Across the Akia Terrane and to its north, zircon morphologies support a complex history of magmatic and metamorphic growth, resorption, and recrystallization through the Mesoarchean from 3240 to 2860 Ma (Friend and Nutman, 1994; Kirkland et al., 2018a; Gardiner et al., 2019). Specifically, temperature estimates of up to (and possibly exceeding) 900 ˚C from our phase equilibrium modelling permit thermally activated volume diffusion of Pb to be viable processes affecting zircon (e.g. Cherniak and Watson, 2001). Evidence for radiogenic-Pb loss, in U–Pb age data and zircon morphologies, is very common in zircon from Mesoarchean orthogneiss of the Akia Terrane (Friend and Nutman, 1994; Garde et al., 2012b; Kirkland et al., 2018a; Gardiner et al., 2019). The spectrum of Pb loss is inconsistent with being related only to a c. 3000 Ma bolide impact, as Pb loss both pre-dates (by up to 200 Ma) and significantly postdates (by up to 140 Ma) the proposed event. The timing of Mesoarchean metamorphism and anatexis also overlaps the timing of magma crystallization, which is consistent with 'automatamorphism' during ongoing magmatic growth. Finally, granulite-facies metamorphism in the Akia terrane also occurs to the south of the Maniitsoq region (Fig. 1; Friend and Nutman, 1994; Garde et al. 2000), which is inconsistent with a local metamorphic event but compatible with a regional high-temperature event.

Tonalite in the Akia Terrane have zircon crystallization ages that range from 3.06 to 2.98 Ga (Garde 1997; Garde et al., 2000; Gardiner et al., 2019) compatible with the minimum timing (based on zircon crystallization ages in leucosome) of high-temperature–low-pressure granulite metamorphism from 3.02 to 2.98 Ga in the Akia terrane (Garde 2007; Garde et al., 2000; this study). A similar duration of tonalite crystallization is recorded in the Fennoscandian Shield from 2.92 to 2.83 Ga and was interpreted to record intracrustal TTG formation in a mafic plateau environment (Laurent et al., 2019). In the Akia terrane, zircon and monazite geochronology from orthogneiss and meta-andesite at Qussuk yield ages of 2995–2975 Ma that were interpreted to record the timing of upper amphibolite metamorphism (Garde et al., 2012b; Scherstén and Garde, 2013), which is consistent with the timing of high-temperature metamorphism and partial melting elsewhere in the Akia terrane. Considering that the trace element modelling of metabasite anatexis reproduces most of the tonalite compositions (Fig. 7) at the inferred temperatures of peak metamorphism and in the immediately underlying crust, tonalite magmatism can be genetically linked to partial melting of the metabasite. The > 40 My duration of the high-temperature thermal event at c. 3.0 Ga suggests a prolonged heat source. We speculate that the generation of tonalite and co-production of dense residue at the base of the crust was rapidly followed by residue delamination; this potentially provided a mechanism to maintain elevated heat flow from the mantle into the crust (c.f. Bédard, 2006; Sizova et al., 2018) especially if there was a long-lived mantle upwelling, which has been proposed for other Archean cratons (Bédard,

2018).

Field relationships support a geodynamic model involving crustal melting by stagnant-lid or extensional magmatism (i.e. no penetrative deformation associated with ca 3.0 Ga metamorphism). Such field evidence is also consistent with the zircon morphologies and age data that support prolonged high-temperature processes. There is no systematic change in the timing of Mesoarchean granulite-facies metamorphism across the western portion of the Akia terrane (Fig. 1), which is inconsistent with the lateral accretion of crustal blocks with different tectonometamorphic histories. Hf-isotope data from zircon suggest that magmatic addition largely occurred through reworking of existing crust with limited input from mantle melting (Gardiner et al., 2019). Hence, the voluminous magmatism derived from reworking of Akia Terrane crust at *c.* 3.0 Ga may have been in a stagnant lid or possibly extensional tectonic environment prior to latest Mesoarchean collisional orogenesis at < 2.98 Ga (Garde, 2007; Friend and Nutman, 2019).

7. Conclusions

Mesoarchean (c. > 3.02–2.98 Ga) granulite-facies metamorphism and partial melting without associated penetrative ductile deformation occurred during the addition of tonalitic magma, consistent with metamorphism during ongoing magmatic accretion at c. 3.0 Ga in the Akia Terrane of the North Atlantic Craton. Phase equilibrium modelling indicates temperatures of at least 800 °C at < 0.8 GPa at the current exposed crustal level, consistent with a high thermal gradient and thin crust. Tonalite is probably derived from slightly deeper in the crust in the garnet stability field at 0.9 GPa and may be related to partial melting of the base of thinned mafic crust. Together, the high apparent thermal gradient and implied thin crust, lack of pervasive penetrative deformation, long-durations (> 40 Ma) at high temperatures, and potential crustal sources of contemporaneous tonalite suggest that Mesoarchean (c. 3.0 Ga) metamorphism in the Akia terrane occurred in a stagnant (or extensional) tectonic regime prior to Neoarchean compressional tectonism.

Declaration of Competing Interest

The authors declare that they have no known competing financial interests or personal relationships that could have appeared to influence the work reported in this paper.

Appendix A. Supplementary data

Supplementary data to this article can be found online at https://doi.org/10.1016/j.precamres.2020.105615.

References

Allaart, J.H., 1982. Frederikshåb Isblink – Søndre Stromfjord. Geological map of Greenland 1:500,000 Scale. The Geological Survey of Greenland.

Bartoli, O., 2017. Phase equilibria modelling of residual migmatites and granulites: An evaluation of the melt-reintegration approach. J. Metamorph. Geol. 35, 919–942.

Bea, F., Montero, P., Ortega, M., 2006. A LA–ICP–MS evaluation of Zr reservoirs in common crustal rocks: implications for Zr and Hf geochemistry, and zircon-forming processes. Canadian Mineral. 44, 693–714.

Bédard, J.H., 2006. A catalytic delamination-driven model for coupled genesis of Archaean crust and sub-continental lithospheric mantle. Geochim. Cosmochim. Acta 70, 1188–1214.

Bédard, J.H., 2018. Stagnant lids and mantle overturns: Implications for Archaean tectonics, magmagenesis, crustal growth, mantle evolution, and the start of plate tectonics. Geosci. Front. 9, 19–49.

Bédard, J.H., Harris, L.B., Thurston, P.C., 2013. The hunting of the snArc. Precambr. Res. 229, 20–48.

Belousova, E.A., Kostitsyn, Y.A., Griffin, W.L., Begg, G.C., O'Reilly, S.Y., Pearson, N.J., 2010. The growth of the continental crust: constraints from zircon Hf-isotope data. Lithos 119, 457–466.

Berthelsen, A., 1962. Structural studies on the pre-Cambrian of western Greenland III. Southern Sukkertoppen district. Bull Gronlands Geol. Undersogelse 31, 47.

Black, L.P., Gulson, B.L., 1978. The age of the Mud Tank carbonatite, Strangways Range, Northern Territory. BMR J. Aust. Geol. Geophys. 3, 227–232.

Black, L.P., Kamo, S.L., Allen, C.M., Davis, D.W., Aleinikoff, J.N., Valley, J.W., Mundil, R., Campbell, I.H., Korsch, R.J., Williams, I.S., Foudoulis, C., 2004. Improved ^{206}Pb/^{238}U microprobe geochronology by the monitoring of a trace-element-related matrix effect; SHRIMP, ID–TIMS, ELA–ICP–MS and oxygen isotope documentation for a series of zircon standards. Chem. Geol. 205, 115–140.

Brown, C.R., Yakymchuk, C., Brown, M., Fanning, C.M., Korhonen, F.J., Piccoli, P.M., Siddoway, C.S., 2016. From source to sink: Petrogenesis of Cretaceous anatectic granites from the Fosdick migmatite–granite complex, West Antarctica. J. Petrol. 57, 1241–1278.

Brown, M., Averkin, Y.A., McLellan, E.L., Sawyer, E.W., 1995. Melt segregation in migmatites. J. Geophys. Res. Solid Earth 100, 15655–15679.

Brown, M., 2013. Granite: From genesis to emplacement. Geol. Soc. Am. Bull. 125, 1079–1113.

Brown, M., Johnson, T., 2018. Secular change in metamorphism and the onset of global plate tectonics. Am. Mineral. 103, 181–196.

Cherniak, D.J., Watson, E.B., 2001. Pb diffusion in zircon. Chem. Geol. 172, 5–24.

Clemens, J., Vielzeuf, D., 1987. Constraints on melting and magma production in the crust. Earth Planet. Sci. Lett. 86, 287–306.

Clemens, J.D., Stevens, G., Farina, F., 2011. The enigmatic sources of I-type granites: the peritectic connexion. Lithos 126, 174–181.

Condie, K.C., Aster, R.C., van Hunen, J., 2016. A great thermal divergence in the mantle beginning 2.5 Ga: Geochemical constraints from greenstone basalts and komatiites. Geosci. Front. 7, 543–553.

Currie, C.A., Hyndman, R.D., 2006. The thermal structure of subduction zone back arcs. J. Geophys. Res. B: Solid Earth 111.

Dhuime, B., Hawkesworth, C.J., Cawood, P.A., Storey, C.D., 2012. A Change in the Geodynamics of Continental Growth 3 Billion Years Ago. Science 335, 1334–1336.

Diener, J., Powell, R., 2010. Influence of ferric iron on the stability of mineral assemblages. J. Metamorph. Geol. 28, 599–613.

Dyck, B., Reno, B.L., Kokfelt, T.F., 2015. The Majorqaq Belt: A record of Neoarchaean orogenesis during final assembly of the North Atlantic Craton, southern West Greenland. Lithos 220, 253–271.

Dymek, R.F., 1984. Supracrustal rocks, polymetamorphism, and evolution of the SW Greenland Archean Gneiss Complex. In: Holland, H.D., Trendall, A.F. (Eds.), Patterns of Change in Earth Evolution. Springer Berlin Heidelberg, Berlin, Heidelberg, pp. 313–343.

Dziggel, A., Diener, J.F.A., Kolb, J., Kokfelt, T.F., 2014. Metamorphic record of accretionary processes during the Neoarchaean: the Nuuk region, southern West Greenland. Precambr. Res. 242, 22–38.

Forshaw, J.B., Waters, D.J., Pattison, D.R., Palin, R.M., Gopon, P., 2019. A comparison of observed and thermodynamically predicted phase equilibria and mineral compositions in mafic granulites. J. Metamorph. Geol. 37, 153–179.

Friend, C.R.L., Nutman, A.P., 1994. Two Archaean granulite-facies metamorphic events in the Nuuk-Maniitsoq region, southern West Greenland: correlation with the Saglek block, Labrador. J. Geol. Soc. London 151, 421–424.

Friend, C.R., Nutman, A.P., 2019. Tectono-stratigraphic terranes in Archaean gneiss complexes as evidence for plate tectonics: the Nuuk region, southern West Greenland. Gondwana Res. 72, 213–237.

Friend, C.R.L., Nutman, A.P., 2005. New pieces to the Archaean terrane jigsaw puzzle in the Nuuk region, southern West Greenland: steps in transforming a simple insight into a complex regional tectonothermal model. J. Geol. Soc. London 162, 147–162.

Friend, C.R.L., Nutman, A.P., Baadsgaard, H., Kinny, P.D., McGregor, V.R., 1996. Timing of late Archaean terrane assembly, crustal thickening and granite emplacement in the Nuuk region, southern West Greenland. Earth Planet. Sci. Lett. 142, 353–365.

Garde, A.A., 1990. Thermal granulite-facies metamorphism with diffuse retrogression in Archaean orthogneisses, Fiskefjord, southern West Greenland. J. Metamorph. Geol. 8, 663–682.

Garde, A.A., 1997. Accretion and evolution of an Archaean high-grade grey gneiss-amphibolite complex: the Fiskefjord area, southern West Greenland. Geol. Greenland Survey Bull. 17.

Garde, A.A., Larsen, O., Nutman, A.P., 1986. Dating of late Archaean crustal mobilisation north of Qugssuk, Godthåbsfjord, southern West Greenland. Rapp. Grønl. Geol. Unders. 128, 23–36.

Garde, A.A., Jensen, S.B., Marker, M. 1987. Field work in the Fiskefjord area, southern West Greenland. Rapport Grøn- lands Geologiske Undersøgelse 135, pp. 36–42.

Garde, A.A., Friend, C., Nutman, A., Marker, M., 2000. Rapid maturation and stabilisation of middle Archaean continental crust: the Akia terrane, southern West Greenland. Bull. Geol. Soc. Den. 47, 1–27.

Garde, A.A., 2007. A mid-Archaean island arc complex in the eastern Akia terrane, Godthåbsfjord, southern West Greenland. J. Geol. Soc. 164 (3), 565–579.

Garde, A.A., Dyck, B., Esbensen, K.H., Johansson, L., Möller, C., 2014. The Finnefjeld domain, Maniitsoq structure, West Greenland: differential rheological features and

mechanical homogenisation in response to impacting? Precambr. Res. 255, 791–808.

Garde, A.A., McDonald, I., Dyck, B., Keulen, N., 2012a. Searching for giant, ancient impact structures on Earth: the Mesoarchaean Maniitsoq structure, West Greenland. Earth Planet. Sci. Lett. 337–338, 197–210.

Garde, A.A., Whitehouse, M., Christensen, R., 2012b. Mesoarchean epithermal gold mineralization preserved at upper amphibolite-facies grade, Qussuk, Southern West Greenland. Econ. Geol. 107, 881–908.

Gardiner, N.J., Kirkland, C.K. Hollis, J., Szilas, K., Steenfelt, A., Yakymchuk, C., Heide-Jørgensen, H., 2019. Building Mesoarchaean crust upon Eoarchaean roots: the Akia Terrane, West Greenland. Contrib. Mineral. Petrol. 174 (20).

Gerya, T.V., Perchuk, L.L., Burg, J.P., 2008. Transient hot channels: perpetrating and regurgitating ultrahigh-pressure, high-temperature crust–mantle associations in collision belts. Lithos 103, 236–256.

Green, E.C.R., White, R.W., Diener, J.F.A., Powell, R., Holland, T.J.B., Palin, R.M., 2016. Activity–composition relations for the calculation of partial melting equilibria in metabasic rocks. J. Metamorph. Geol. 34, 845–869.

Hamilton, W.B., 2011. Plate tectonics began in Neoproterozoic time, and plumes from deep mantle have never operated. Lithos 123, 1–20.

Hanson, G.N., 1978. The application of trace elements to the petrogenesis of igneous rocks of granitic composition. Earth Planet. Sci. Lett. 38, 26–43.

Hartel, T.H.D., Pattison, D.R.M., 1996. Genesis of the Kapuskasing (Ontario) migmatitic mafic granulites by dehydration melting of amphibolite: the importance of quartz to reaction progress. J. Metamorph. Geol. 14, 591–611.

Hastie, A.R., Kerr, A.C., McDonald, I., Mitchell, S.F., Pearce, J.A., Wolstencroft, M., Millar, I.L., 2010. Do Cenozoic analogues support a plate tectonic origin for Earth's earliest continental crust? Geology 38, 495–498.

Herzberg, C., Rudnick, R., 2012. Formation of cratonic lithosphere: An integrated thermal and petrological model. Lithos 149, 4–15.

Holland, T.J.B., Powell, R., 2011. An improved and extended internally consistent thermodynamic dataset for phases of petrological interest, involving a new equation of state for solids. J. Metamorph. Geol. 29, 333–383.

Holness, M.B., Sawyer, E.W., 2008. On the pseudomorphing of melt-filled pores during the crystallization of migmatites. J. Petrol. 49, 1343–1363.

Jackson, S.E., Pearson, N.J., Griffin, W.L., Belousova, E.A., 2004. The application of laser ablation-inductively coupled plasma-mass spectrometry to in situ U-Pb zircon geochronology. Chem. Geol. 211, 47–69.

Jamieson, R.A., Beaumont, C., 2013. On the origin of orogens. GSA Bull. 125, 1671–1702.

Janousek, V., Moyen, J.F., 2019. Whole-rock geochemical modelling of granite genesis–the current state of play. Geological Society, London, Special Publications 491, SP491-2018.

Johnson, T.E., Brown, M., Gardiner, N.J., Kirkland, C.L., Smithies, R.H., 2017. Earth's first stable continents did not form by subduction. Nature 543, 239–242.

Johnson, T.E., Brown, M., Kaus, B.J., VanTongeren, J.A., 2014. Delamination and recycling of Archaean crust caused by gravitational instabilities. Nat. Geosci. 7, 47–52.

Kelsey, D.E., Clark, C., Hand, M., 2008. Thermobarometric modelling of zircon and monazite growth in melt-bearing systems: examples using model metapelitic and metapsammitic granulites. J. Metamorph. Geol. 26, 199–212.

Keulen, N., Garde, A.A., Jørgart, T., 2015. Shock melting of K-feldspar and interlacing with cataclastically deformed plagioclase in granitic rocks at Toqqusap Nunaa, southern West Greenland: implications for the genesis of the Maniitsoq structure. Tectonophysics 662, 328–344.

Kirkland, C.L., Yakymchuk, C., Hollis, J., Heide-Jørgensen, H., Danišík, M., 2018a. Mesoarchean exhumation of the Akia terrane and a common Neoarchean tectonothermal history for West Greenland. Precambr. Res. 314, 129–144.

Kirkland, C.L., Yakymchuk, C., Szilas, K., Evans, N., Hollis, J., McDonald, B., Gardiner, N.J., 2018b. Apatite: a U-Pb thermochronometer or geochronometer? Lithos 318–319, 143–157.

Kirkland, C., Slagstad, T., Johnson, T., 2018c. Zircon as a metamorphic timekeeper: a case study from the Caledonides of central Norway. Gondwana Res. 61, 63–72.

Kohn, M.J., Corrie, S.L., Markley, C., 2015. The fall and rise of metamorphic zircon. Am. Mineral. 100, 897–908.

Korhonen, F., Clark, C., Brown, M., Bhattacharya, S., Taylor, R., 2013. How long-lived is ultrahigh temperature (UHT) metamorphism? constraints from zircon and monazite geochronology in the Eastern Ghats orogenic belt, India. Precambr. Res. 234, 322–350.

Laurent, O., Vander Auwera, J., Bingen, B., Bolle, O., Gerdes, A., 2019. Building up the first continents: Mesoarchean to Paleoproterozoic crustal evolution in West Troms, Norway, inferred from granitoid petrology, geochemistry and zircon U-Pb/Lu-Hf isotopes. Precambr. Res. 321, 303–327.

Liou, P., Guo, J., 2019. Generation of archaean TTG gneisses through amphibole-dominated fractionation. J. Geophys. Res. Solid Earth 124, 3605–3619.

Ludwig, K., 2003. User's manual for IsoPlot 3.0. A Geochronological Toolkit for Microsoft Excel 71.

Ludwig, K. 2009. SQUID 2: A User's Manual, rev. 12 Apr, 2009. Berkeley Geochron. Ctr. Spec. Pub. 5 110 p.

Martin, H., Moyen, J.F., Guitreau, M., Blichert-Toft, J., Le Pennec, J.L., 2014. Why Archaean TTG cannot be generated by MORB melting in subduction zones. Lithos 198, 1–13.

McDonough, W.F., Sun, S.S., 1995. The composition of the Earth. Chem. Geol. 120, 223–253.

McGregor, V.R., Friend, C.R.L., 1992. Late Archean prograde amphibolite-to granulite-facies relations in the Fiskenæsset region, southern West Greenland. J. Geol. 100, 207–219.

McGregor, V.R., Friend, C.R.L., 1997. Field recognition of rocks totally retrogressed from granulite facies: an example from Archaean rocks in the Paamiut region, South-West Greenland. Precambr. Res. 86, 59–70.

Mole, D.R., Barnes, S.J., Le Vaillant, M., Martin, L.A.J., Hicks, J., 2018. Timing, geochemistry and tectonic setting of Ni-Cu sulfide-associated intrusions of the Halls Creek Orogen, Western Australia. Lithos 314, 425–446.

Moyen, J.-F., Laurent, O., 2018. Archaean tectonic systems: a view from igneous rocks. Lithos 302–303, 99–125.

Moyen, J.-F., Martin, H., 2012. Forty years of TTG research. Lithos 148, 312–336.

Nagel, T.J., Hoffmann, J.E., Münker, C., 2012. Generation of Eoarchean tonalite-trondhjemite-granodiorite series from thickened mafic arc crust. Geology 40, 375–378.

Nutman, A.P., Christiansen, O., Friend, C.R., 2007. 2635 Ma amphibolite facies gold mineralisation near a terrane boundary (suture?) on Storø, Nuuk region, southern West Greenland. Precambr. Res. 159, 19–32.

Nutman, A.P., Friend, C.R., Hiess, J., 2010. Setting of the ~2560 Ma Qôrqut Granite complex in the Archean crustal evolution of southern west Greenland. Am. J. Sci. 310, 1081–1114.

Nutman, A.P., Friend, C.R., 2007. Adjacent terranes with ca. 2715 and 2650 Ma high-pressure metamorphic assemblages in the Nuuk region of the North Atlantic Craton, southern West Greenland: complexities of Neoarchaean collisional orogeny. Precambr. Res. 155, 159–203.

Palin, R.M., Dyck, B., 2018. Metamorphic consequences of secular changes in oceanic crust composition and implications for uniformitarianism in the geological record. Geosci. Front. 9, 1009–1019.

Palin, R.M., White, R.W., Green, E.C., 2016a. Partial melting of metabasic rocks and the generation of tonalitic–trondhjemitic–granodioritic (TTG) crust in the Archaean: Constraints from phase equilibrium modelling. Precambr. Res. 287, 73–90.

Palin, R.M., White, R.W., Green, E.C., Diener, J.F., Powell, R., Holland, T.J., 2016b. High-grade metamorphism and partial melting of basic and intermediate rocks. J. Metamorph. Geol. 34, 871–892.

Palin, R.M., Weller, O.M., Waters, D.J., Dyck, B., 2016c. Quantifying geological uncertainty in metamorphic phase equilibria modelling; a Monte Carlo assessment and implications for tectonic interpretations. Geosci. Front. 7, 591–607.

Patiño Douce, A.E., Beard, J.S., 1995. Dehydration-melting of biotite gneiss and quartz amphibolite from 3 to 15 kbar. J. Petrol. 36, 707–738.

Paton, C., Hellstrom, J., Paul, B., Woodhead, J., Hergt, J., 2011. Iolite: Freeware for the visualisation and processing of mass spectrometric data. J. Anal. At. Spectrom. 26, 2508–2518.

Polat, A., Wang, L., Appel, P.W., 2015. A review of structural patterns and melting processes in the Archean craton of West Greenland: evidence for crustal growth at convergent plate margins as opposed to non-uniformitarian models. Tectonophysics 662, 67–94.

Powell, R., Holland, T.J.B., 1988. An internally consistent dataset with uncertainties and correlations: 3. Applications to geobarometry, worked examples and a computer program. J. Metamorph. Geol. 6, 173–204.

Rapp, R.P., Watson, E.B., Miller, C.F., 1991. Partial melting of amphibolite/eclogite and the origin of Archean trondhjemites and tonalites. Precambr. Res. 51, 1–25.

Reichardt, H., Weinberg, R.F., 2012. Hornblende chemistry in meta- and diatexites and its retention in the source of leucogranites: an example from the Karakoram shear zone, NW India. J. Petrol. 53, 1287–1318.

Ricjputi, L.R., Valley, J.W., McGregor, V.R., 1990. Conditions of Archean granulite metamorphism in the Godthab-Fiskenaesset region, southern West Greenland. J. Metamorph. Geol. 8, 171–190.

Rudnick, R.L., Gao, S., 2014. 4.1 – Composition of the Continental Crust A2 – Holland, Heinrich D. In: Turekian, K.K. (Ed.), Treatise on Geochemistry, Second ed. Elsevier, Oxford, pp. 1–51.

Sawyer, E.W., 1987. The role of partial melting and fractional crystallization in determining discordant migmatite leucosome compositions. J. Petrol. 28 (3), 445–473.

Sawyer, E.W., 1999. Criteria for the recognition of partial melting. Phys. Chem. Earth Part A 24, 269–279.

Scherstén, A., Garde, A.A., 2013. Complete hydrothermal re-equilibration of zircon in the Maniitsoq structure, West Greenland: A 3001 Ma minimum age of impact? Meteorit. Planet. Sci. 48, 1472–1498.

Sizova, E., Gerya, T., Brown, M., Perchuk, L.L., 2010. Subduction styles in the Precambrian: insight from numerical experiments. Lithos 116, 209–229.

Sizova, E., Gerya, T., Brown, M., Stüwe, K., 2018. What drives metamorphism in early Archean greenstone belts? insights from numerical modeling. Tectonophysics 746, 587–601.

Sizova, E., Gerya, T., Stüwe, K., Brown, M., 2015. Generation of felsic crust in the Archean: a geodynamic modeling perspective. Precambr. Res. 271, 198–224.

Smithies, R.H., Van Kranendonk, M.J., Champion, D.C., 2005. It started with a plume–early Archaean basaltic proto-continental crust. Earth Planet. Sci. Lett. 238, 284–297.

Stacey, J.S., Kramers, J.D., 1975. Approximation of terrestrial lead isotope evolution by a two-stage model. Earth Planet. Sci. Lett. 26, 207–221.

Steiger, R.H., Jäger, E., 1977. Subcommission on geochronology: convention on the use of decay constants in geo- and cosmochronology. Earth Planet. Sci. Lett. 36, 359–362.

Stern, R.A., Bodorkos, S., Kamo, S.L., Hickman, A.H., Corfu, F., 2009. Measurement of SIMS instrumental mass fractionation of Pb isotopes during zircon dating. Geostand. Geoanal. Res. 33, 145–168.

Stevens, G., Villaros, A., Moyen, J.F., 2007. Selective peritectic garnet entrainment as the origin of geochemical diversity in S-type granites. Geology 35, 9–12.

Stuck, T.J., Diener, J.F., 2018. Mineral equilibria constraints on open-system melting in metamafic compositions. J. Metamorph. Geol. 36, 255–281.

Szilas, K., Tusch, J., Hoffmann, J.E., Garde, A.A., Münker, C., 2017. Hafnium isotope constraints on the origin of Mesoarchaean andesites in southern West Greenland, North Atlantic craton. Geol. Soc., London, Spec.Publ. 449, 19–38.

Tedeschi, M.T., Hagemann, S.G., Kemp, A.I.S., Kirkland, C.L., Ireland, T.R., 2019.

Geochronological constrains on the timing of magmatism, deformation and mineralization at the Karouni orogenic gold deposit: Guyana, South America. Precambr. Res. https://doi.org/10.1016/j.precamres.2019.04.015.

van Kranendonk, M.J., 2010. Two types of Archean continental crust: plume and plate tectonics on early Earth. Am. J. Sci. 310, 1187–1209.

White, R.W., Pomroy, N.E., Powell, R., 2005. An in situ metatexite–diatexite transition in upper amphibolite facies rocks from Broken Hill, Australia. J. Metamorph. Geol. 23, 579–602.

White, R.W., Powell, R., 2002. Melt loss and the preservation of granulite facies mineral assemblages. J. Metamorph. Geol. 20, 621–632.

White, R.W., Powell, R., Halpin, J.A., 2004. Spatially-focussed melt formation in aluminous metapelites from Broken Hill, Australia. J. Metamorph. Geol. 22, 825–845.

White, R.W., Palin, R.M., Green, E.C., 2017. High-grade metamorphism and partial melting in Archean composite grey gneiss complexes. J. Metamorph. Geol. 35, 181–195.

Winther, T., Newton, R.C., 1991. Experimental melting of hydrous low-K tholeiite: evidence on the origin of Archaean cratons. Bull. Geol. Soc. Den. 39, 213–228.

Wyman, D., 2013. A critical assessment of Neoarchean "plume only" geodynamics: evidence from the Superior Province. Precambr. Res. 229, 3–19.

Wyman, D., 2018. Do cratons preserve evidence of stagnant lid tectonics? Geosci. Front. 9, 3–17.

Yakymchuk, C., 2019. On granites. J. Geol. Soc. India 94, 9–22.

Yakymchuk, C., Brown, M., 2014a. Consequences of open-system melting in tectonics. J. Geol. Soc. London 171, 21–40.

Yakymchuk, C., Brown, M., 2014b. Behaviour of zircon and monazite during crustal melting. J. Geol. Soc. London 171, 465–479.

Yakymchuk, C., Brown, M., 2019. Divergent behaviour of Th and U during anatexis: implications for the thermal evolution of orogenic crust. J. Metamorph. Geol. 37, 899–916.

Yakymchuk, C., Clark, C., White, R.W., 2017. Phase relations, reaction sequences and petrochronology. Rev. Mineral. Geochem. 83, 13–53.

Yakymchuk, C., Zhao, W., Wan, Y., Lin, S., Longstaffe, F.J., 2019. Fluid-present anatexis of Neoarchean tonalite and amphibolite in the Western Shandong Province. Lithos 326, 110–124.